The role of snow-surface coupling, radiation, and turbulent mixing in modeling a stable boundary layer over Arctic sea ice

H. A. M. Sterk,[1] G. J. Steeneveld,[1] and A. A. M. Holtslag[1]

[1]   To enhance the understanding of the impact of small-scale processes in the polar climate, this study focuses on the relative role of snow-surface coupling, radiation and turbulent mixing in an Arctic stable boundary layer. We extend the GABLS1 (GEWEX Atmospheric Boundary-Layer Study 1) model intercomparison for turbulent mixing with the other relevant physical processes in the stable boundary layer over sea ice. We use the Single Column Model (SCM) version of the Weather Research and Forecasting (WRF) mesoscale meteorological model and run different combinations of boundary layer and radiation schemes, using a state-of-the art land surface scheme. With this intercomparison of schemes, we confirm a wide variety in the state of the atmosphere and the surface variables for the selected parameterization schemes. To understand this variety, a sensitivity analysis for one particular combination of parameterization schemes is performed, using a novel analysis method of process diagrams. The variation between the sensitivity runs indicates a relative orientation of model sensitivities to variations in each of the governing processes and these can explain the variety of model results obtained in the intercomparison of different parameterization schemes. Moreover, we apply the same method for several geostrophic wind speeds to represent a large range of synoptic conditions. Results indicate a shift in process significance for different wind regimes. For low wind regimes, the model sensitivity is larger for surface coupling and radiation, while for high wind speeds, the largest sensitivity is found for the turbulent mixing process. An interesting non-linear feature was found for turbulent mixing for frequently occurring wind speeds and low wind speed cases, where the 2 m temperature increases for decreased amounts of mixing.

1.   Introduction

[2] Modeling the atmospheric stable boundary layer (SBL) is a challenging task. Many global and regional climate model outputs diverge from one another, as well as from observations for near-surface variables such as temperature, wind speed, and humidity (see also section 2). These features underline the lack of understanding of the governing mechanisms related to the SBL. Furthermore, SBL modeling may be hampered by computational limitations such as resolution. The relatively coarse resolution that is often used in operational models is typically not sufficient to represent the SBL properly [e.g., *Steeneveld et al.*, 2006b; *Svensson and Holtslag*, 2009]. However, a good representation of the SBL is important for numerical weather prediction [*Beljaars and Viterbo*, 1998; *Viterbo et al.*, 1999; *Atlaskin and Vihma*, 2012], air quality studies [*Hanna and Yang*, 2001; *Salmond and McKendry*, 2005], understanding polar biogeochemistry [*Hunke and Meier*, 2012], and climate modeling [*Tjernström et al.*, 2005; *Holtslag et al.*, 2007].

[3] The SBL is affected by many small-scale physical processes, such as turbulent mixing, the coupling of the atmosphere and the underlying medium, radiation, the presence of clouds or fog, subsidence, advection, gravity waves, and drainage and katabatic flows [*Delage*, 1997; *Mahrt et al.*, 1998; *Mahrt*, 1999; *Steeneveld* et al., 2006b]. The ongoing challenges in SBL modeling are related to the physical processes and their interactions, which are either not completely understood, or are represented incompletely. To enhance the understanding and representation of the SBL in regional and large-scale models, so far three GABLS (GEWEX Atmospheric Boundary Layer Study) experiments have been organized [*Holtslag*, 2006; *Holtslag et al.*, 2012].

[4] We build upon the GABLS1 experiment for which a large eddy simulation (LES) [*Beare et al.*, 2006] and a single column model (SCM) intercomparison study [*Cuxart et al.*, 2006] have been performed, set on a weakly SBL over ice. These studies indicated that LES models and most SCMs are able to simulate a weakly SBL, but that operational models typically have too much mixing. Both studies were performed with a prescribed surface temperature and surface cooling. However, in reality, the surface temperature, sensible

[1]Meteorology and Air Quality Section, Wageningen University, Wageningen, The Netherlands.

Corresponding author: H. A. M. Sterk, Meteorology and Air Quality Section, Wageningen University, PO Box 47, 6700 AA, Wageningen, The Netherlands. (marina.sterk@wur.nl)

heat flux, and ice/soil heat flux are strongly interdependent [*Derbyshire*, 1999] and the surface temperature will be affected through a coupled surface energy budget [*Holtslag and de Bruin*, 1988; *Duynkerke*, 1991; *van de Wiel et al.*, 2002; *Steeneveld et al.*, 2006a]. Therefore, it is important to consider the coupling between the surface and the lower atmosphere in SBL modeling.

[5] In addition to the feedbacks in this nonlinear coupled system, the surface temperature and sensible heat flux are strongly dependent on the geostrophic wind regime [*Steeneveld et al.*, 2006a, 2006b; *Holtslag et al.*, 2007]. Roughly speaking, we can distinguish between two SBL types. Type I represents the very stable case where the system is dominated by radiative cooling and low wind speeds and has a more exponentially (or concave up) shaped potential temperature (θ) profile ($\partial^2\theta/\partial z^2 < 0$), while type II is typical for larger wind speeds, and therefore has a well-mixed (or concave down) vertical θ profile ($\partial^2\theta/\partial z^2 > 0$) [*Van Ulden and Holtslag*, 1985; *Vogelezang and Holtslag*, 1996]. Considering the Arctic SBL, the ERA-Interim reanalysis data for the years 1979–2010 indicates that a wide variety of the 850 hPa wind field (as a proxy for the geostrophic wind speed) occurs for the regions above 75°N for the NH winter (Figure 1), and it is likely that both SBL regimes can be found. We will study the different wind regimes in this paper.

[6] The overall aim of this study is to examine which of the governing processes in the Arctic SBL are most dominant in explaining the SBL state for different wind regimes. Here we focus on the processes of snow-surface coupling (also known as conductive heat flux), radiation and turbulent mixing, since these processes are controlling the evolution and structure of the SBL the most [*André and Mahrt*, 1982; *Beljaars and Holtslag*, 1991; *Steeneveld et al.*, 2006b; *Bosveld et al.*, 2012]. Utilizing the WRF (Weather Research and Forecasting) SCM, first the model will be run with different parameterization schemes for the representation of the SBL and the longwave radiative effects. In this way, the model output variability between parameterization
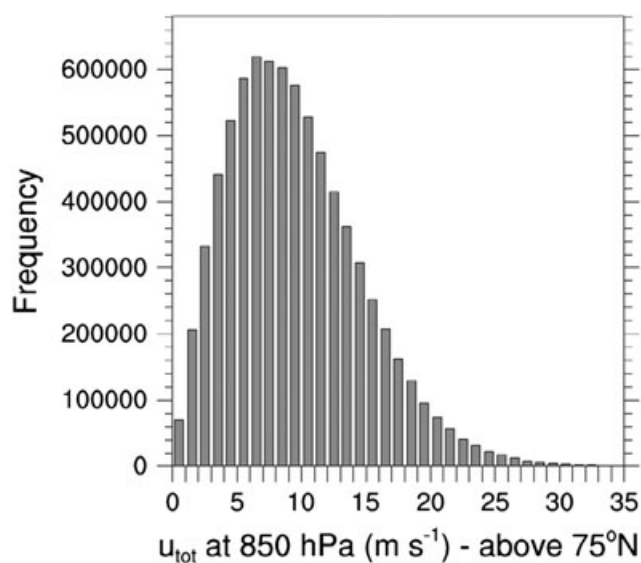
schemes within one mother model can be explored. Second, after selecting one permutation of schemes, a sensitivity analysis will be performed for the main processes, using novel process diagrams as introduced by *Bosveld et al.* [2012] for GABLS3. This approach illustrates for which processes the model is more sensitive and which physical processes can explain the model variability and hence where future research efforts should be focused. Finally, we investigate whether errors in the boundary layer (BL) schemes can remain hidden by compensating errors in another part of the model such as the land surface scheme. Hence, this study is not a validation study of the WRF parameterization schemes, but a strategic study to determine possible focus points for future research. Therefore, apart from adjusting an incorrectly implemented stability function as well as a limitation for the friction velocity in the YSU BL scheme, we apply the schemes in the WRF 3.2.1. model without any modifications or tuning, despite that these schemes might have produced some biases in earlier model evaluations for both homogeneous or complex terrain. For instance, the 2 m temperatures (T_{2m}) have been reported as either too warm or too cold [*Hu et al.*, 2010; *Tastula and Vihma*, 2011; *Mäkiranta et al.*, 2011; *Shin and Hong*, 2011]. Also wind speed was found to be either overestimated [*Tastula and Vihma*, 2011; *Shin and Hong*, 2011] or underestimated [*Mäkiranta et al.*, 2011], while the overall correlation coefficients for wind speed are rather low, especially under low wind speeds [*Tastula and Vihma*, 2011; *Mäkiranta et al.*, 2011]. Furthermore, some complications can occur with the surface layer formulation which can only handle a limited range of stabilities, e.g., by a lower limit for the friction velocity u* [*Jiménez et al.*, 2011]. However, these uncertainties in the model performance underline the need for a sensitivity analysis within WRF.

[7] As mentioned before, our study is based on the GABLS1 benchmark [*Beare et al.*, 2006; *Cuxart et al.*, 2006], but extended to coupling with the land/snow surface and by comparing the importance of the processes for different geostrophic wind speeds. To exclude vertical resolution as a limiting factor, we will use a vertical resolution in the atmosphere which is much higher than in GABLS1.

[8] The paper is organized as follows: section 2 provides more background information for this study, particularly on the challenges in modeling the Arctic stable boundary layer. Section 3 gives a model description with an overview of the utilized parameterization schemes. Section 4 describes the GABLS1 case as we use it, and this is applied in the model intercomparison in section 5 and the sensitivity analysis in sections 6 and 7. This is followed by the conclusion and discussion in section 8.

Figure 1. Histogram of ERA-Interim 850 hPa wind speeds (ms^{-1}) for latitudes > 75°N for the months of December, January, and February of years 1979–2010.

2. Background

[9] The last few decades the Arctic region seems subject to rapid changes. Available observations report an increase of the surface air temperature in a large part of the Arctic [*Johannessen et al.*, 2004]. At the same time, the sea ice cover decreases rapidly, e.g., in 2007 the observed sea ice autumn minimum was 38% smaller than the climatological mean of 1979–2007 [*Comiso et al.*, 2008]. Additional changes such as retreating glaciers and the thawing of permafrost are reported [*ACIA*, 2005].

[10] The mentioned observations indicate that the Arctic climate system is more sensitive to climate change than the lower latitudes, a feature known as "Arctic amplification" (AA) [*Serreze and Francis*, 2006; *Bony et al.*, 2006], of which the physical origin is so far not completely understood. A possible explanation for the AA is that several feedbacks in the polar climate system may enhance the initial response. The ice-albedo feedback [*Curry et al.*, 1995], for example, enhances the Arctic warming. In addition, changes in cloud cover and water vapor can contribute to AA [*Graversen and Wang*, 2009]. Other contributors are, e.g., changes in oceanic and atmospheric circulation and the weak vertical mixing in the Arctic lower atmosphere [*Alexeev et al.*, 2005; *Graversen et al.*, 2008; *Graversen and Wang*, 2009]. Furthermore, the amount of horizontal and vertical mixing affects the efficiency at which the effects of local warming diffuse to adjacent regions [*Serreze et al.*, 2011]. *Bintanja et al.* [2011a, 2011b] found that with a stronger surface inversion, the surface warming signal dilutes less easily aloft and thus remains at the surface, consequently further enhancing the temperature. This feature is important especially in the Arctic winter, where strong surface inversions occur frequently, and indicates the significance of the θ profile.

[11] Using Surface Heat Budget of the Arctic Ocean (SHEBA) tower data, *Persson et al.* [2002] found that the mean near-surface conditions are strongly stable from November to April, although hourly data did reveal neutral stratifications occurring 25% of the time in winter with clouds and higher wind speeds. From the same data, *Grachev et al.* [2005, 2007] found bulk Richardson numbers (Ri_B) mostly greater than 0, frequently greater than the critical Ri_B and sometimes even greater than 1. Furthermore, the stability parameter z/L could reach up to 100. SHEBA soundings indicated near surface stratified conditions 61% and 53% of the time in autumn and winter respectively [*Tjernström and Graversen*, 2009].

[12] Despite earlier research efforts, SBL modeling remains challenging, which particularly arises during model intercomparison and evaluation studies. As an illustration, the ensemble mean of regional climate models in *Rinke et al.* [2006] provides T_{2m} that are up to 5 K too cold compared to the European Centre for Medium-Range Weather Forecasts (ECMWF) reanalysis data in winter, while the scatter between the models was 1–5 K over land. *Holland and Bitz* [2003] compared several coupled atmosphere-ocean-sea-ice-land models. The simulations for doubled CO_2 concentrations showed a range of warming for the Arctic between 1.7 and 4.3 times the global average, with some up to even 9 K warmer. Moreover, *Walsh et al.* [2008] report area-averaged annual root mean square errors of surface air temperature of 15 global climate models compared to ERA40 reanalysis data of 3 to almost 14 K for the Arctic region. Note that although these reanalysis data are used as a reference in these studies, they can have some inefficiencies of their own, since due to limited observations in these regions, the reanalyses are mostly based on model parameterizations [e.g., *Tjernström and Graversen*, 2009], but these can have serious problems in dealing with the physical processes in this region.

[13] In addition to the T_{2m} biases, deficiencies are found in the modeled inversion strengths. *Boé et al.* [2009], defining the inversion strength between 850 and 1000 hPa, compared 15 CMIP3 models which showed an average inversion strength in the range of 2.1–7.4 K for November to February. On the contrary, defining the inversion strength as the temperature change across the BL gives a mean inversion strength of about 13 K for the SHEBA data in stably stratified cases in autumn and winter [*Tjernström and Graversen*, 2009]. Although the results from observations represent surface-based inversion layers and have a higher vertical resolution, the differences with the models do indicate that these inversion strengths are not captured properly by the models (which also follows from the differences between the models), although in cases of surface pressure higher than 1000 hPa the actual inversion strength can be stronger than mentioned in the study of *Boé et al.* [2009].

[14] To gain further understanding in modeling the Arctic SBL, we examine the relative strength of the governing processes in the SBL during cooling conditions and under various wind regimes. First, we consider the coupling between the snow surface and the lower atmosphere which plays a distinct role in the SBL [*Holtslag and De Bruin*, 1988; *Duynkerke*, 1991; *van de Wiel et al.*, 2002; *Steeneveld et al.*, 2006a; *Holtslag et al.*, 2007]. The surface temperature (T_{surf}), sensible heat flux, and soil/ice/snow heat flux are strongly interdependent [*Derbyshire*, 1999] and can influence the SBL evolution. The soil heat flux is determined by the soil's thermal heat conductivity and temperature gradient and influences the energy flux to the atmosphere. Implementing a skin layer in the surface model does improve the model performance substantially [*Holtslag and De Bruin*, 1988; *Steeneveld et al.*, 2006a, 2006b], since it allows T_{surf} to react more easily to sudden changes in the surface cooling [*van de Wiel et al.*, 2002; *Steeneveld et al.*, 2006a]. In our study, the underlying medium is ice, which is covered by a snow layer which will act as an insulation layer. The area of the snow cover and its depth control the land-atmosphere coupling and affect the air and the soil/ice temperature [*Dutra et al.*, 2011]. They should thus be accounted for.

[15] Second, we study the relative impact of longwave radiation, which has two distinct effects on the SBL [*Edwards*, 2009]. The first is that the net radiation at the surface dominates T_{surf} and is greatly influenced by conditions in and above the SBL, for example, by clouds [e.g., *Intrieri et al.*, 2002; *Stramler et al.*, 2011]. Moreover, the divergence of longwave radiative flux across the SBL can affect its development [*Edwards*, 2009] and also takes place in clear-sky nighttime conditions, because of the presence of absorbing gases, e.g., water vapor, CO_2, O_3, and aerosols [*Garratt and Brost*, 1981; *André and Mahrt*, 1982]. *Tjemkes and Duynkerke* [1989] found that including radiative cooling in the atmosphere acts to reduce the inversion strength across the BL, making the BL less stable, and increasing the SBL height by 25%. Also *Hoch et al.* [2007] note the importance of the longwave radiative flux divergence during the ETH Summit Greenland experiment and report radiative cooling of typically $10–20 \, \text{K} \, \text{d}^{-1}$.

[16] Finally, we also study turbulent mixing, which is in principle determined by the stratification and wind shear. In clear-sky conditions, the stratification suppresses the buoyancy and turbulence is solely produced by wind shear. Therefore, the vertical structure of both wind and θ strongly influences the SBL state. In the very stable case with very little turbulence, turbulent transport between the surface and the overlying atmosphere vanishes, and the net radiation

equals the soil heat flux. This can result in a so-called "decoupled" state of the SBL and is also seen in observations [*Derbyshire*, 1999; *Grachev et al.*, 2005]. From a modeler's perspective, then the SBL's decoupled state may result in unrealistically cold surface temperatures [*Derbyshire*, 1999; *Jiménez et al.*, 2011]. To circumvent this model phenomenon, some large-scale models utilize artificial enhanced mixing or enhanced thermal diffusion for very stable situations [e.g., *Viterbo et al.*, 1999].

3. Model Description

[17] The single column model (SCM) in our study is based on the WRF 3D model version 3.2.1. The WRF SCM uses the same physics and dynamics as the WRF 3D model [*Skamarock et al.*, 2008], and a few features will be highlighted here. The model utilizes a vertically stretched σ coordinate, with the model top defined at a constant pressure surface.

[18] The WRF model has a wide range of parameterizations for several physical processes, which differ in their degree of complexity and computation time. In our study, we examine the relative importance of the coupling with the surface, the radiative effects, and the turbulent mixing. The following sections will briefly describe the selected land/snow-surface, the longwave radiation, and the BL parameterizations.

3.1. Snow Surface Coupling

[19] The land surface models (LSMs) provide the fluxes of the energy balance: the sensible, latent and soil heat flux, and the upward longwave and shortwave radiation. As such, the LSMs provide the lower boundary condition for the vertical transport in the BL scheme. Additionally, they determine the skin temperature (T_{skin}), the temperature and moisture profiles in the soil, as well as the snow cover and canopy properties [*Skamarock et al.*, 2008].

[20] In this study, we use the Noah LSM as a reference [*Chen and Dudhia*, 2001; *Ek et al.*, 2003]. This model uses four layers to represent the dynamics in the soil (ice). The layer thicknesses in our setup are from top to bottom 1, 2, 4, and 8 cm (see section 4). The Noah LSM can handle soil, ice, and fractional snow cover effects and considers surface emissivity properties [*Skamarock et al.*, 2008]. Snow effects are included in just the top soil layer. Thus, the thickness of the top layer is defined as the thickness of the top soil/ice layer plus the snow depth. The thermal conductivity of the top layer is then defined as the weighted sum of the product of the thermal conductivity and layer thickness of the individual layers [*Ek et al.*, 2003].

3.2. Longwave Radiation

[21] In addition to the land surface physics, the longwave radiative transport needs to be parameterized. The radiation schemes represent the atmospheric cooling due to radiative flux divergence and determine the amount of downward longwave and shortwave radiation at the surface [*Skamarock et al.*, 2008]. In our study, a 9 h run during polar nighttime is performed and therefore we study only longwave radiation (LW$_{rad}$). The LW$_{rad}$ scheme considers thermal radiation that is absorbed and emitted by gases, water species, and the land/snow surface [e.g., *Rodgers*, 1967]. To determine LW$_{rad}$, the scheme takes the model-forecasted cloud and water vapor distributions into account, as well as specified concentrations of CO_2, O_3, and optionally trace gases.

[22] Ideally, radiative transfer models can use the line-by-line approach, where the absorption and emission are calculated for each wavelength. This approach, however, is computationally expensive and more often the broad band or correlated k method is used. The latter uses several bands of wavelengths for which averaged values of absorption and emission are employed. This approach limits the computation time and is within 1% accuracy compared to the line-by-line approach [*Stensrud*, 2007].

[23] Three different LW$_{rad}$ schemes are used in this study. The first scheme is the Rapid Radiative Transfer Model (RRTM) [*Mlawer et al.*, 1997], which is used as the reference scheme. This is a spectral-band scheme with 16 different bands [*Skamarock et al.*, 2008]. The scheme treats several molecular species, namely water vapor, CO_2, O_3, CH_4, N_2O, and the common halocarbons, and accounts for cloud optical depth.

[24] The second LW$_{rad}$ scheme is the Eta Geophysical Fluid Dynamics Laboratory (GFDL) scheme. For this scheme, the radiation spectrum is divided into 14 bands, which treat water vapor, CO_2, and O_3 in its calculations [*Skamarock et al.*, 2008].

[25] The last LW$_{rad}$ scheme that has been selected is the spectral-band scheme used in the NCAR Community Atmosphere Model (CAM). CAM has only two bands in the longwave range. As well as the RRTM and the GFDL scheme, it treats water vapor, CO_2, and O_3. Furthermore, the CAM scheme accounts for several trace gases [*Collins et al.*, 2004; *Skamarock et al.*, 2008].

3.3. Turbulent Mixing

[26] The boundary layer (BL) schemes parameterize the sub-grid scale turbulent fluxes of heat, momentum, and moisture throughout the atmospheric column. The schemes that are used in this study are either a relatively simple first or a more complex one-and-a-half order closure.

[27] The first scheme that we have selected is the so-called YSU BL scheme [*Hong et al.*, 2006; *Skamarock et al.*, 2008]. This is a first-order scheme that uses profiles for the eddy diffusivities of heat, momentum, and moisture in terms of friction velocity and the BL depth following *Troen and Mahrt* [1986] and *Holtslag and Boville* [1993] among many others. The BL top depends on the buoyancy profile by using a critical bulk Richardson number (Rib_{cr}) to determine the BL height. In stable conditions, $Rib_{cr} = 0.25$ is applied over land. It appears that in this way, enhanced mixing is allowed under weak geostrophic winds [*Mauritsen et al.*, 2007; *Hong and Kim*, 2008]. Note that in the YSU scheme as implemented in WRF 3.2.1, the stability function ϕ was not correctly implemented (Sukanta Basu and Wayne Angevine, personal communications, summer 2012). As such we have replaced the erroneous function by the intended version: $\phi = 1 + 5z/L$ (as in the original *Troen and Mahrt* [1986] description), which leads to less enhanced mixing compared to the original YSU scheme. This implementation also makes the runs compatible with WRF 3.4.1.

[28] In addition, we consider the Mellor-Yamada-Janjic (MYJ) BL scheme [*Mellor and Yamada*, 1982]. The MYJ scheme is a local, 1.5 order closure model and is considered appropriate for stable and slightly unstable flows, but the

errors can increase when the atmosphere becomes more convective [*Hu et al.*, 2010].

[29] The third BL scheme that we consider is the Quasi-Normal Scale Elimination (QNSE) scheme [*Sukoriansky et al.*, 2006]. The eddy diffusivities for heat, momentum, and moisture are estimated using an alternative approach, which accounts for the combined effects of turbulence and waves. Moreover, this scheme accounts for anisotropy, which is especially relevant in the SBL where vertical motions are suppressed. In addition, the scheme does not have a Ri_{cr} at which turbulence is suppressed, and turbulence can thus exist even at very high Ri. In practice, QNSE was implemented as a modification of the MYJ scheme and is also a local, 1.5 order closure model. Good agreement was found between the QNSE scheme and observations for cases of moderate and strong stable stratification [*Sukoriansky et al.*, 2006].

[30] Together with the BL scheme, the surface layer scheme is used. This scheme determines the friction velocities and the exchange coefficients, which are provided both to the land surface model and the BL scheme to enable the calculation of the fluxes of the energy balance at the surface and the surface stress respectively [*Skamarock et al.*, 2008]. In WRF, each BL scheme has a particular surface layer scheme tied to it. For YSU, this is the MM5 surface scheme, which makes use of Monin-Obukhov similarity theory. For MYJ, the ETA surface layer scheme is applied, which is also based on the Monin-Obukhov similarity theory [*Tastula and Vihma*, 2011]. Also for the QNSE BL scheme, its analogue surface layer scheme has been utilized [*Sukoriansky*, 2008].

4. Case Description

[31] Our study has been inspired by the GABLS1 SCM intercomparison study which is based on the LES study of the Arctic SBL by *Kosovic and Curry*, 2000, but with some modifications. They used the Beaufort Sea Arctic Stratus Experiment observational data set to define the initial and boundary conditions. These were chosen such that a clear-sky SBL with moderate surface cooling could be numerically simulated. The case was also used for an LES and 1D intercomparison study [*Beare et al.*, 2006, *Cuxart et al.*, 2006] to analyze the reliability of LES and 1D models for the SBL. For these experiments, the cooling rate was prescribed, which is a limiting boundary condition, and the radiation schemes were switched off.

[32] We adopt the same initial profiles of potential temperature (θ) and wind speed as in the GABLS1 case study. The θ profile consists of a 100 m thick mixed layer of $\theta = 265$ K. Above this layer, θ increases at a rate of 0.01 K m^{-1}. The geostrophic wind speed (u_{geo}) was chosen as 8 ms^{-1} for the u component and 0 ms^{-1} for the v component. Below 100 m, the wind speed decreases logarithmically to 0 ms^{-1} at the surface (z_{0m}). Figure 1 reveals that a u_{geo} of 7–8 ms^{-1} indeed occurs most frequently in the Arctic. The specific humidity profile (q) has a uniform value of $q_0 = 0.5$ gkg^{-1} up to a height of 4 km. This is comparable to what was found from observations, e.g., *Serreze et al.* [1995] found a value of $q_0 \sim 0.8$ gkg^{-1} during winter above 70°N, while near-surface q_0 from SHEBA winter data was found to range between 0.1 and 0.7 gkg^{-1} [*Tjernström et al.*, 2005; *Stramler et al.*, 2011]. Above 4 km to the model

top, which is at 12 km, q decreases exponentially according to $q_0 \cdot \exp(-\alpha(z - 4000m))$, where $\alpha = 10^{-3}$. To overcome a large amount of degrees of freedom and because we want to focus on the interaction of the snow surface and the SBL, we decided to keep the atmosphere clear from clouds and turned the microphysics off. The impact of the microphysics might also be important since cloudy conditions also frequently occur in the Arctic which can affect the Arctic surface energy balance [e.g., *Intrieri et al.*, 2002; *Shupe and Intrieri*, 2004]. Therefore, this impact needs to be studied on its own in a subsequent study.

[33] The GABLS1 case uses a rather large roughness length (z_0) for snow/ice of 0.1 m for momentum and heat. Although we are aware that usually the thermal roughness length is smaller than the roughness length for wind speed [*Andreas*, 1987], a thermal roughness parameterization is not included in this WRF model, and we apply a roughness length of 5×10^{-4} m for both momentum and heat, since this is more in agreement with observed roughness lengths. For example, from the ASFG tower at SHEBA, z_0 was found to be about $3.1 - 10.8 \times 10^{-4}$ m [*Persson et al.*, 2002], while *Schröder et al.* [2003] report an average z_0 of 5×10^{-4} m for a wide range of sea ice conditions. z_0 Measured at six SHEBA winter sites [*Andreas et al.*, 2010] ranged from 10^{-7} to 10^{-1} m.

[34] The WRF model uses a lower limit on u_* of 0.1 m s^{-1} in the YSU BL scheme to prevent a vanishing heat flux in very stable conditions [*Jiménez et al.*, 2011]. Otherwise, this could possibly cause a decoupling between the atmosphere and the surface resulting in too low temperatures at the surface. However, in very stable conditions, this u_* minimum is rather high, therefore we set it to 0.001 m s^{-1} to reduce the restriction, but still preventing the heat flux from becoming zero and therefore avoid runaway cooling [*Jiménez et al.*, 2011]. Finally, the case runs at 73°N latitude with a time step of 10 s, has a duration time of 9 h, and is performed in wintertime to ascertain the total absence of solar heating at the surface.

[35] In the current study, the SBL is modeled with a very high vertical atmospheric resolution. In this way we can focus on the relative significance of the representation of the physical processes without a limiting vertical resolution playing a role. We chose 200 vertical levels in the atmosphere, which were stretched so that the thinnest layer is closest to the surface, and the layer thickness increases with height. The first model level is located at about 0.55 m. Since now the first model level is below the 2 m level, we had to interpolate T_{2m} from the temperature profile, as the standard WRF T_{2m} uses T_{skin} in combination with the exchange coefficients (see equation (4)) as determined at the 2 m level and not the temperature difference between the model level above and below 2 m, which is in disagreement with the profile.

[36] *Steeneveld et al.* [2006a] showed that the model results are very sensitive to the vertical resolution in the ice when the atmosphere and surface are coupled. In order to obtain a better interaction with the ice, the thickness of the layers as in the original Noah LSM is reduced. The ice slabs are now, respectively, from the top to bottom layer 1, 2, 4, and 8 cm thick. The initial temperature profile for the ice layers is set to a uniform value of 265 K. The ice is fully covered by a 5 cm snow layer which is the snow depth as in the WRF SCM for sea ice. Since during the winter night this

snow depth might be a bit low, we reran the model with 20 cm snow depth and will briefly comment on that as well. The emissivity of a fresh snow surface is 0.98 and is comparable to what was found in observations [*Kondo and Yamazawa*, 1986; *Claffey et al.*, 1999; *Persson et al.*, 2002; *Andreas et al.*, 2010]. The total ice thickness is 3 m for multi-year sea ice, and the lower boundary condition for temperature at the ice-water interface is 271.16 K in the Noah LSM in WRF.

5. Model Intercomparison

[37] In this section, the boundary layer (BL) and radiation (LW$_{rad}$) schemes are varied (see section 3). As such, the spread between the permutations is quantified, which reflects the uncertainties that can occur within one model.

[38] First, we compare the forecasted θ profiles after 9 h (Figure 2a, the initial profile is given as well). This figure shows the profound difference in shape of the θ profiles. The runs with the MYJ scheme indicate an exponentially shaped profile, while the YSU and QNSE runs provide some mixing as is also seen from the inflection point in the profile, though they do show a strong inversion. For the YSU scheme, this inversion is smoother, while for the QNSE a strong inversion is seen on top of the shallow "mixed" layer. Consequently, the figure reveals that both SBL "archetypes" as mentioned in the introduction can be obtained by choosing different BL schemes, even with the same wind forcings, where YSU and QNSE can be allocated the type II SBL and MYJ type I. The difference between MYJ and QNSE is explained by the allowed turbulent mixing under extreme stable conditions in QNSE, while this is absent in MYJ [*Sukoriansky et al.*, 2006].

[39] Examining the first model level temperatures, MYJ runs cool the least with a cooling from 265 K to ~250.5 K, while YSU runs cool to ~249 K. The coldest first model level temperatures are found for the QNSE runs, with $\theta \sim 248.8$ K. Thus after 9 h, the model runs produce a spread of almost 2 K near the surface.

[40] While the differences between the BL schemes can be clearly distinguished, the differences between the three LW$_{rad}$ schemes are small for the θ profiles. For example,

the incoming longwave radiation ($L\downarrow$) for similar BL schemes differs ~3 Wm^{-2} after 9 h, on a total amount of $L\downarrow$ of about 168 Wm^{-2}.

[41] Due to the large differences in θ profiles, it might be more meaningful to compare the amount of integrated cooling (*IC*) as a measure for the temperature differences, since for a better mixed profile, the cooling at the surface might not be as strong, but aloft more cold air is found. The *IC* is defined as [*Steeneveld et al.*, 2006a]

$$IC = \int_{z=0}^{z=200m} (\theta_{start} - \theta_{final})dz \qquad (1)$$

[42] Here we only calculate the *IC* up to 200 m, since this is the height where the model runs converge. Table 1 presents the *IC* for the model intercomparison runs. Although the MYJ runs show the least cooling at the first model level, the *IC* is the largest, because of the relatively colder air above ~33 m compared to the other BL schemes. The YSU and QNSE runs show a similar cooling at the first model level, but the integrated cooling is larger for the QNSE runs, which reflects a more effective mixing of cold air into the atmosphere.

[43] The wind profiles also show some differences (Figure 2b), especially between the MYJ runs and the other BL schemes. The MYJ runs forecast a more smooth wind profile and a low level jet at ~85 m. The YSU and QNSE runs do not show such a clear low level jet and reach their maximum wind speed at a lower altitude. As for the θ profile

Table 1. Integrated Cooling for the Model Intercomparison Runs

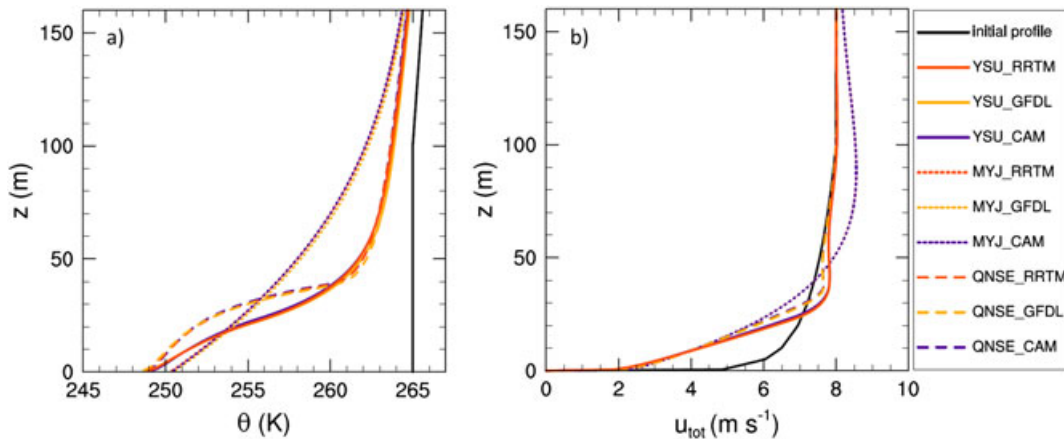| BL Scheme	LWrad Scheme	IC (K m)
YSU	RRTM	−653
YSU	GFDL	−633
YSU	CAM	−665
MYJ	RRTM	−925
MYJ	GFDL	−896
MYJ	CAM	−931
QNSE	RRTM	−734
QNSE	GFDL	−716
QNSE	CAM	−745

Figure 2. Vertical structure of (a) the potential temperature θ (K) and (b) the total wind speed u_{tot} (ms^{-1}) for various WRF SCM runs, initially and after 9 h.

and the IC, also for the wind profiles the largest differences occur between the BL schemes. Thus, at first sight, the BL scheme seems to be most important in explaining the differences between the model runs. However, in the next section, we will analyze whether there may be complementary processes at hand which can show a similar spread.

6. Sensitivity and Process Analyses

[44] To analyze and quantify which of the three governing processes of snow-surface coupling, radiation, and turbulent mixing is most critical in determining the state of the SBL, we perform an extensive sensitivity and process analysis. To do so, we chose the YSU BL scheme as a reference, because this scheme is a first-order scheme and allows for some enhanced mixing, while for the LW_{rad} scheme, RRTM was chosen. Both schemes are close to operational practice in weather forecasts and climate modeling [*Iacono et al.*, 2000; *Morcrette et al.*, 2001; *Roeckner et al.*, 2003; *Collins et al.*, 2004; *Cuxart et al.*, 2006; *Inoue et al.*, 2006; *ECMWF*, 2009, 2012].

[45] The amount of coupling of the surface to the atmosphere is affected by adjusting the snow/ice conductivity λ. The amount of incoming longwave radiation ($L\downarrow$) is changed by adjusting the initial specific humidity profile (q). *Svensson and Karlsson* [2011] found that it is primarily the q profile and not the temperature profile that determines the clear-air $L\downarrow$ in very cold and dry conditions and hence that the atmospheric moisture content is very important for the radiation balance at the Arctic surface. Results by *Zhang et al.* [2001] also indicated that changes in the atmospheric precipitable water have a higher impact on $L\downarrow$ than the change in mean atmospheric temperature. Finally, the amount of turbulent mixing is varied by both adjusting the eddy diffusivity coefficient for heat, momentum, and moisture K in the BL scheme, and the exchange coefficients C for heat, momentum, and moisture in the LSM to adjust the mixing in the surface layer. Note that in *Bosveld et al.* [2012] only the activity of turbulent mixing above the lowest level was adjusted. However, it is more physical to consistently link the surface layer and the BL as was also recognized by *Svensson and Holtslag* [2009]. To more easily compare our results with those of *Bosveld et al.* [2012], we also show the mixing sensitivity analysis while only adjusting K in the BL scheme.

[46] To study how the changes in process strengths compare to one another, we will show a series of plots as introduced by *Bosveld et al.* [2012] for the GABLS3 intercomparison study. In this paper, we refer to these plots as "process diagrams." A process diagram plots two variables against each other, which are either a time average of variable X over 9 h, or a change of variable X in 9 h time. Therefore, each model run is represented by one point in the process diagram. The points for the model intercomparison runs performed in the previous section give the spread within the WRF SCM. From the point for the reference run with the YSU-RRTM scheme combination, we will add the points for the sensitivity analysis runs. By drawing lines from the reference point to these sensitivity points, we can compare the direction of the sensitivity for a certain process and indicate whether this might explain the spread within the WRF SCM. Furthermore, we can compare the orientation

and length of these lines under different geostrophic wind regimes (u_{geo}) to learn how the relative significance of the physical processes shifts. To compare the significance of the three processes for varying u_{geo} in a more convenient way, the axes of the cross-plots representing different u_{geo} are kept identical. Finally, we extend *Bosveld et al.* [2012] by carrying out two perturbations in each "direction" (e.g., two runs with increased mixing, two runs with decreased mixing) to detect whether the change in process intensity gives a linear response (straight line) or a nonlinear response (curved line).

[47] Below we study the sensitivity for a prescribed amplification of the coefficients described above, while in section 7 we compare runs with a similar change in the net surface energy budget. The extended GABLS1 case with $u_{geo} = 8 \text{ ms}^{-1}$ will be used as a reference case when we compare the competition between the physical processes for different ranges of u_{geo}. Figure 1 shows that this wind speed is often found at latitudes north of 75°N. The case is repeated for a u_{geo} of 3 and 20 ms^{-1} to cover a wide variety of wind speeds in the Arctic (see also Figure 1).

6.1. Amplification Strategy

[48] In the first part of the sensitivity analysis, we prescribe the amplification of the governing processes. These multiplication factors were chosen to get a significant effect in the sensitivity analysis. To increase the amount of coupling, we multiplied the ice/snow conductivity (λ) with 2.0 and 4.0. To decrease the amount of coupling, a multiplication factor of 0.5 and 0.25 was applied. These runs are referred to as *coupling*. The rationale behind these multiplication factors are the large uncertainties observed in λ_{snow} and λ_{ice}, which can vary in space (both horizontally and vertically) and time due to density and texture differences for example. *Sturm et al.* [2002] report in situ measurements of λ_{snow} during the SHEBA experiment ranging from 0.078 to 0.574 Wm^{-1}K^{-1} with the lowest values for fresh snow and the highest value for a layer of snow-ice. From these probe measurements, they found an average bulk λ of 0.14 Wm^{-1}K^{-1}, while when they used measured ice growth to deduce the heat extraction from the ice and hence determine the bulk λ, values of 0.1–0.7 Wm^{-1}K^{-1} were found with an average of 0.34 Wm^{-1}K^{-1}, but this also includes the effect of heterogeneity. *Huwald et al.* [2005] calculated an effective λ_{snow} at the snow-ice interface by using the SHEBA internal snow and ice temperature data and found hourly values that ranged from 0.1 to 1.0 Wm^{-1}K^{-1}, while the average values ranged from 0.4 to 0.5 Wm^{-1}K^{-1}. Other studies also show a range of 0.02–0.3 Wm^{-1}K^{-1} for various sites [*Gouttevin et al.*, 2012] and 0.06–0.4 Wm^{-1}K^{-1} for various depths [*Domine et al.*, 2012]. With a set λ of about 0.22 Wm^{-1}K^{-1} in the WRF SCM, λ in our sensitivity analysis ranges from 0.055 to 0.88 Wm^{-1}K^{-1} when we use the multiplication factors of 0.25–4.0.

[49] Large variations are also found in the modeled incoming longwave radiation ($L\downarrow$). *Svensson and Karlsson* [2011] revealed that the median for $L\downarrow$ during the Arctic winter (DJF) ranged from about 140 to 190 Wm^{-2} for nine global climate models. Although this contains all sky conditions, the range in variation for $L\downarrow$ in clear-sky conditions was also found to be over 20 Wm^{-2}. When we would use identical multiplication factors as for λ to vary the initial q profiles (*radiation* runs),

the initial specific humidity profile would range up to $2\,\mathrm{g\,kg^{-1}}$ which is rather high for an Arctic winter (see also section 4). Therefore, we decided to multiply with 0.5, 0.67, 1.5, and 2.0. In this way, we can still compare the 0.5 and 2.0 perturbations in a systematic approach with the other sensitivity analyses, while representing typical Arctic conditions better. The $L\!\downarrow$ after 9 h now ranges between 155.2 and $180.3\,\mathrm{Wm^{-2}}$ compared to the $167.4\,\mathrm{Wm^{-2}}$ of the reference run.

[50] To alter the amount of mixing, the eddy diffusivity K in the BL scheme and the exchange coefficient C in the LSM are again multiplied with 0.25–4.0. These runs are referred to as *mixing*. For the mixing sensitivity analysis as was applied in *Bosveld et al.* [2012] only K in the BL scheme was varied. Since the maximum eddy diffusivities for heat and momentum that were found in the SCM intercomparison study by *Cuxart et al.* [2006, see their Figure 6) ranged from less than 1 to over $5\,\mathrm{m^2\,s^{-1}}$, we anticipate that the range of the multiplication factors covers the typical uncertainty in K.

6.2. Vertical Profiles

[51] We start discussing the sensitivity analysis for $u_{\mathrm{geo}} = 8\,\mathrm{ms^{-1}}$ (a frequently occurring wind speed, see Figure 1). Figures 3a and 3b show the θ and wind speed profile after a 9 h forecast for the YSU-RRTM reference run and for the sensitivity analysis runs for this u_{geo}. Also the initial profiles are presented for comparison. The labels K_Chm, K, λ, and q represent the processes of mixing in both BL and surface layer, mixing in only the BL, snow-surface coupling, and radiation, respectively, and the numbers indicate the amount by which each process is multiplied.

[52] An increase in mixing leads to higher temperatures at the surface, since there is more entrainment of potential warmer air from the overlying layers and cold air from the surface is more easily lifted aloft so that there is a more efficient redistribution of heat in the boundary layer. This also results in deeper and better mixed boundary layers. Similar results were found for increasing the amount of snow-surface coupling. An increased λ means that heat from the underlying and relatively warmer ice layers is more efficiently transported to the surface and thus more energy is added to the atmosphere. An increased q results in a higher amount of $L\!\downarrow$. This again leads to higher temperatures and deeper boundary layers compared to the YSU-RRTM reference run. Also we observe that applying a multiplication factor of 0.5 and 2.0 for both coupling and radiation forecasts comparable profiles. When the physical processes are decreased in intensity, results change in opposite directions.

[53] Some differences can be observed between both types of mixing runs. When we increase the amount of mixing, the boundary layers are deeper and better mixed when the amount of mixing is also increased in the surface layer (K_Chm runs). This more effective mixing also follows from the higher amount of integrated cooling for K_Chm runs compared to runs with only mixing in the BL (K runs) (see Table 2). However, when we decrease the amount of mixing, we also find higher atmospheric temperatures for the K_Chm runs compared to the K runs. On the other hand, T_{skin} remains colder for the K_Chm runs compared to the K runs, resulting in large temperature gradients between the surface and the lowest model level for the K_Chm runs (see also Table 2). This is explained by the smaller sensible heat flux in the K_Chm runs which hampers the transport of heat to the surface.

[54] Also when we study the two "decreased mixing" lines of the K_Chm runs, we see that when mixing is increased from $0.25\,K\_Chm$ to $0.5\,K\_Chm$, the temperatures in the atmosphere just above the surface decrease. This behavior is contrary to the expectation that when mixing increases, more warm air is entrained, which would result in higher atmospheric temperatures. It appears that, when the amount of mixing is decreased sufficiently, the cold air from the surface is not effectively lifted and therefore the layers above the surface do not cool as much, while at the same time, the warmer air aloft cannot reach the surface. Indeed, we find lower surface temperatures for the $0.25\,K\_Chm$ run compared to the $0.5\,K\_Chm$ run (see Table 2).

[55] Table 2 summarizes the amount of integrated cooling (*IC*) for the sensitivity analysis runs. The *IC* of the YSU-RRTM reference run amounts up to $-653\,\mathrm{K\,m}$. When we decrease the amount of mixing, the *IC* decreases, because cold air from the surface is not efficiently mixed into the atmosphere. Indeed we find a stronger *IC* for decreased mixing for the K runs compared to K_Chm, where the exchange coefficients in the surface layer are kept identical to the YSU-RRTM reference run so that there is a more efficient mixing of cold air away from the surface. Decreasing the coupling leads to increased *IC*, because of the less efficient heat transport from the deeper ice layers to the surface, enabling the surface to cool more, while the mixing remains strong enough to bring this signal to higher atmospheric layers. Decreasing the amount of $L\!\downarrow$ also leads to lower T_{skin} and again a stronger integrated cooling. Opposite results are found for increasing the process strengths.

[56] The vertical profiles for a u_{geo} of 3 and $20\,\mathrm{ms^{-1}}$ are given in Figures 3c–3f. Note that the axes are different from the figures for $u_{\mathrm{geo}} = 8\,\mathrm{ms^{-1}}$. Increasing u_{geo} results in more developed and deeper SBL heights and overall higher θ as more warm air is mixed toward the surface and cold air is mixed away from the surface.

[57] Reducing u_{geo} results in smaller SBL heights and strongly affects the θ profile. The YSU-RRTM θ profile now has an exponential, or type I, shape. The profile shape remains similar for increased and decreased amounts of $L\!\downarrow$ and coupling, although this does respectively increase and decrease θ. With increased mixing, the θ profile shape becomes somewhat more mixed, although this only happens in a shallow layer. When the mixing decreases in intensity, a pronounced exponential profile is forecasted. As was the case with the smallest amounts of mixing for $u_{\mathrm{geo}} = 8\,\mathrm{ms^{-1}}$, again we note that not only the mean SBL temperatures remain higher when the mixing is decreased, but also now the mean SBL temperatures decrease when the amount of mixing increases. This is likely caused by the small sensible heat flux which prevents the transport of warm air toward the surface and transport of cold air away from the surface.

[58] As mentioned in the introduction, we can distinguish between two types of SBLs. Type I has a more exponential (or concave up) profile and is dominated by radiative cooling and low wind speeds. Type II is typical for larger wind speeds and better mixed (or concave down) vertical temperature profiles [*Van Ulden and Holtslag*, 1985; *Vogelezang and Holtslag*, 1996]. In Figure 3c, the different profile shapes can be observed, although this is not necessarily followed by the lower and higher wind speeds for types I and II, respectively, in Figure 3d. However, this sensitivity analysis does indicate
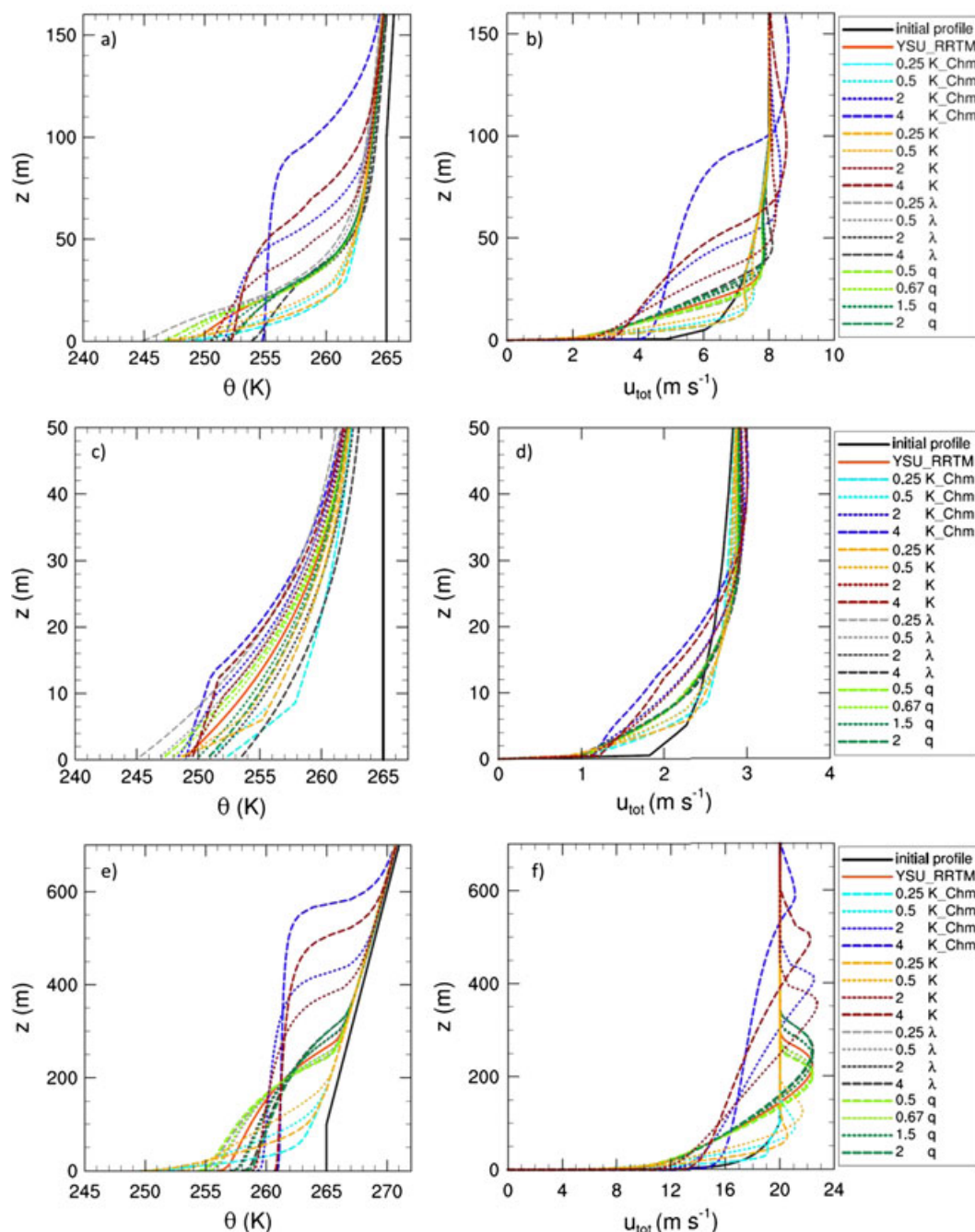
Figure 3. Vertical profiles for (a, c, and e) potential temperature θ (K) and (b, d, and f) wind speed u_{tot} (ms^{-1}) initially and after 9 h forecasts for the runs of the sensitivity analysis using geostrophic wind speeds of (a and b) 8 ms^{-1}, (c and d) 3 ms^{-1}, and (e and f) 20 ms^{-1}. *K_Chm* represents the eddy diffusivity and exchange coefficients and therefore the change in mixing in both boundary and surface layer, *K* represents the eddy diffusivity and therefore change in mixing in the boundary layer only, λ represents the ice conductivity and thus the coupling, and *q* represents the specific humidity profile and therefore the incoming longwave radiation. YSU-RRTM is the reference run.

the importance of parameter choice for the vertical profile for cases of low u_{geo}, since it affects the vertical profile shape significantly.

6.3. Process Diagrams: Snow-Surface Coupling

[59] Figure 4a depicts the process diagram for the T_{2m} cooling that occurs in 9 h and the soil heat flux (G) averaged

over 9 h for $u_{geo} = 8$ ms^{-1}. As such, this figure represents the time-integrated interaction between the surface and the atmosphere. The spread within the WRF SCM results (the runs with sets of different parameterizations shown by the first nine symbols in the legend) shows a small but clear correlation: the stronger the amount of surface cooling, the larger G is. This is explained by the fact that G depends on

Table 2. Overview of the Amount of Integrated Cooling (IC), the 2 m Temperature ($T_{2m\ 9h}$) and Skin Temperature ($T_{skin\ 9h}$) After 9 h for a Geostrophic Wind Speed of 8 ms^{-1}, and the Changes in Net Radiation Over 9 h (ΔQ^*, See Equation (5)) for the Three Wind Regimes for the Sensitivity Analysis Runs

Parameter	Multiplication Factor	IC (K m)	$T_{2m\ 9h}$	$T_{skin\ 9h}$	ΔQ^* (Wm^{-2}) $u_{geo} = 8$ ms^{-1}	ΔQ^* (Wm^{-2}) $u_{geo} = 3$ ms^{-1}	ΔQ^* (Wm^{-2}) $u_{geo} = 20$ ms^{-1}
K_Chm	0.25	−479	250.7	245.5	7.6	4.8	25.7
	0.5	−532	249.5	245.8	5.2	3.4	16.2
	2.0	−893	251.7	250.6	−11.1	−4.2	−11.7
	4.0	−1160	254.8	254.3	−23.4	−8.2	−16.6
K	0.25	−513	248.8	245.9	5.2	2.4	17.5
	0.5	−564	248.8	246.4	3.2	1.3	9
	2.0	−793	250.7	248.7	−4.6	−1.4	−6.8
	4.0	−977	252.3	250.1	−9.8	−3	−10.9
λ	0.25	−787	245.6	243.1	14	15.4	4
	0.5	−727	247.3	245.0	8	8.6	2.3
	2.0	−580	251.9	250.1	−9.1	−9.4	−2.6
	4.0	−521	254.2	252.6	−17.3	−18.3	−5.3
q	0.5	−678	247.3	244.8	−5	−5.2	−6.2
	0.67	−669	248.2	245.8	−2.8	−3	−3.6
	1.5	−628	251	249.1	2.4	3	3.3
	2.0	−601	252.3	250.5	3.6	4.9	5.3

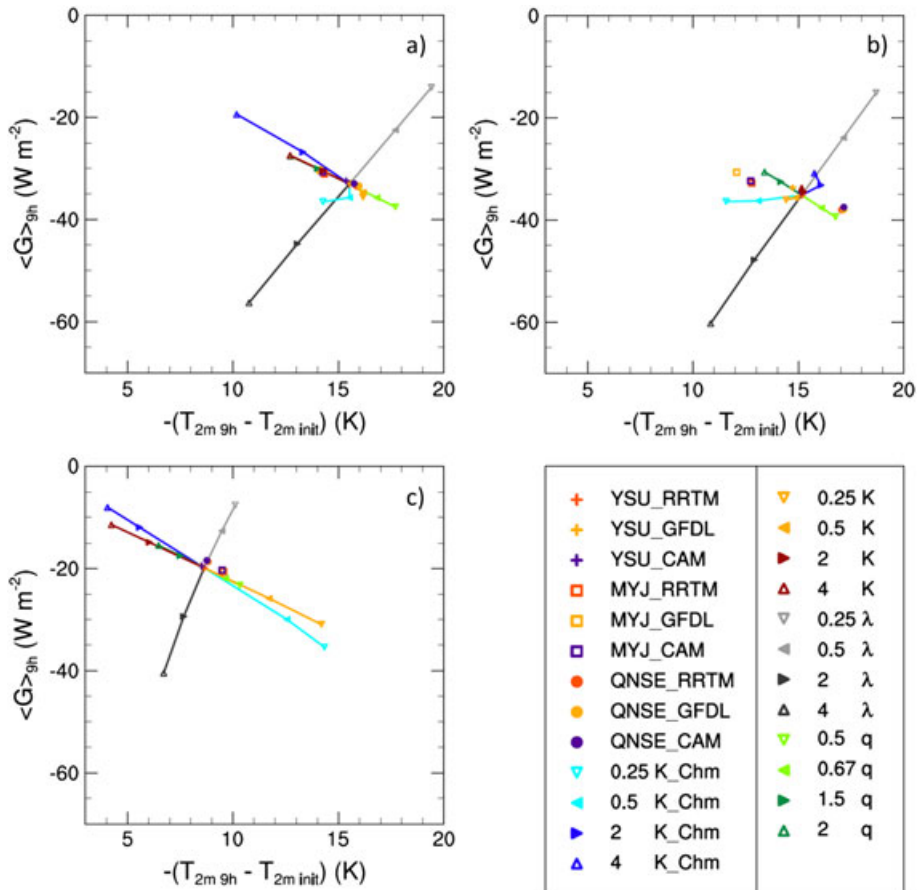**Figure 4.** Cooling of the 2 m temperature ($-(T_{2m\ 9h} - T_{2m\ init})$ (K)) over the 9 h run versus the soil heat flux ($<G>_{9h}$ (Wm^{-2})) averaged over 9 h for a geostrophic wind speed of (a) 8 ms^{-1}, (b) 3 ms^{-1}, and (c) 20 ms^{-1}. K_Chm represents the eddy diffusivity and exchange coefficients and therefore the change in mixing in both boundary and surface layer, K represents the eddy diffusivity and therefore change in mixing in the boundary layer only, λ represents the ice conductivity and thus the coupling, and q represents the specific humidity profile and therefore the incoming longwave radiation. YSU-RRTM is the reference run.

the ice conductivity (λ) and the temperature difference between the surface and the lower ice layers (dT/dz, where z increases downward):

$$G = -\lambda \frac{dT}{dz} \qquad (2)$$

[60] With a stronger atmospheric cooling and a stronger decrease in $T_{\rm skin}$, the upper ice temperature difference increases and that results in a stronger G. This in turn tends to increase $T_{\rm skin}$ which leads to a smaller G. Hence, the process of snow-surface coupling has a negative feedback.

[61] The results of the sensitivity analysis are indicated with the lines. The line of the coupling sensitivity is oriented perpendicular to the orientation of the model intercomparison runs. The reason for this perpendicular orientation is that λ is adjusted to generate more and less coupling. To increase the amount of coupling, λ is increased, which causes a stronger G. Also now more heat from the ice is brought to the surface into the atmosphere resulting in higher $T_{\rm skin}$, which is reflected in higher $T_{\rm 2m}$ and less cooling at this level.

[62] The processes of turbulent mixing and radiation only affect the temperatures at the surface and do not influence λ. When the amount of turbulence increases, more heat is transported to the surface and cold air is transported aloft. An increase in $L\downarrow$ also results in higher $T_{\rm skin}$. Thus both these enhanced process strengths reduce the temperature difference in the ice and result in smaller G. The opposite occurs for a decrease in $L\downarrow$ and for the decreased K runs.

[63] A nonlinear feature is observed for the decreased K_Chm runs, where there is also less mixing in the surface layer, and for runs with K decreased from 0.5 to 0.25. We will come back to this later. The overall direction of the sensitivity lines is comparable with the results of *Bosveld et al*. [2012] for GABLS3, although the direction of our K and q runs shows more overlap.

[64] Since the lines of radiation, and partially mixing, are oriented in the same direction as the spread within the model, they explain mostly the spread within the model for these plotted variables. Furthermore, the overlap indicates that the radiation and mixing processes can compensate each other for this set of variables. The coupling can also compensate these processes as far as $T_{\rm 2m}$ is concerned. In a way this graph is rather straightforward, because to obtain the spread within the models, several BL schemes were used for which the mixing is calculated differently, and several $LW_{\rm rad}$ schemes were used including therefore differences in $L\downarrow$. However, Figure 4 also indicates that surface coupling has a strong influence on the $T_{\rm 2m}$ cooling and G. The difference between the K_Chm and K runs does indicate the sensitivity of the model to the description of the surface layer and its link to the BL in the parameterization schemes.

[65] Figure 4b shows a similar process diagram, but for $u_{\rm geo} = 3\,{\rm ms}^{-1}$. We see that the orientation of the model intercomparison runs is similar as those for $u_{\rm geo} = 8\,{\rm ms}^{-1}$, but with a larger spread. Furthermore, the orientation of the radiation and coupling processes as well as their length, is comparable with those for the standard $u_{\rm geo}$. The line representing turbulent mixing, however, has a different orientation for multiplication factors of 0.5–2.0 and shows a change in direction for the amount of cooling in time as was also seen in the line from 0.5 to 0.25 K_Chm for $u_{geo} = 8\,{\rm ms}^{-1}$. For both types of mixing runs, a decrease in mixing results in less $T_{\rm 2m}$ cooling and a larger G. A possible explanation for this will be given later on. The line does not change direction regarding G. Increasing the amount of mixing does increase $T_{\rm skin}$ (because the cold air is mixed to the air just above the surface). Therefore, the temperature difference between the skin layer and the deeper ice layers decreases, followed by a decrease in G. Furthermore, the model is more sensitive for mixing when this process is also adjusted in the surface layer, since the line for the K_Chm runs is considerably longer than for the K runs.

[66] As far as the orientation of the points is concerned, it is seen that radiation plays a large role in explaining the differences between the model intercomparison runs. This does not come as a large surprise. As can be seen in Figure 3c, the θ profiles resemble a type I profile as in *Vogelezang and Holtslag* [1996], which represents mainly radiation-dominated boundary layers.

[67] Figure 4c presents the results for a wind regime of $20\,{\rm ms}^{-1}$. The orientation of the model intercomparison runs is similar to the 3 and $8\,{\rm ms}^{-1}$ runs and again follows the alignment of the radiation and mixing (K runs) sensitivity as for the $8\,{\rm ms}^{-1}$ case. However, the line representing coupling has decreased in length and is now more "steep": it still covers a large range in the change in average G (which is directly linked to the change in λ), but this does not have as strong an impact on the $2\,{\rm m}$ cooling. The radiation line is similar in length, but the line representing turbulent mixing is now relatively larger and plays a more important role. This is also seen from the stronger change in G and $2\,{\rm m}$ cooling when multiplying both mixing processes by 0.5 and 2.0 compared to multiplying the radiation process with the same factors. The difference in line length for both increased and decreased mixing indicates that the model is more sensitive for decreasing turbulent mixing than an increase in mixing. This is probably related to the fact that if there already is sufficient mixing, an increase in mixing only causes the change in the system to be divided over a deeper BL and the signal may not be as clearly detectable.

[68] In order to study the sensitivity of our results for snow thickness, we repeated the runs for a thicker snow cover of 20 cm. Although the forecasts for the three geostrophic wind speeds resulted in overall colder solutions, the relative orientation of the sensitivity lines remained approximately similar. Especially the insensitivity of coupling for higher wind regimes was now even more pronounced, with a line hardly deviating from the reference run. The same holds for the process diagrams in sections 6.4 and 6.5.

[69] Next, we still need to explain the nonlinearity in the K_Chm sensitivity analysis runs for the 3 and $8\,{\rm ms}^{-1}$ case regarding the amount of cooling at $2\,{\rm m}$. Intuitively, one would expect that, when increasing the amount of mixing, more warm air is redistributed toward the surface. Thus, the amount of cooling in time should decrease for increased mixing and vice versa for a decreased amount of mixing. This is indeed the case for a $u_{\rm geo}$ of $20\,{\rm ms}^{-1}$ and partly for the 3 and $8\,{\rm ms}^{-1}$ regime, but for the other cases opposite results are found.

[70] In fact, similar results were found by *McNider et al*. [2012] in their model study. As they used two different models than the WRF SCM, this gives more confidence in the nonlinear behavior. For low wind speed regimes, they

obtained colder atmospheric solutions when the wind speed was increased. In their study also the two states of the SBL were found. *McNider et al.* explain that for very light wind speeds, there is so little mixing that the boundary layer is very shallow and weak and only a little amount of cold air is mixed from the surface to the first model level. When now the wind speed increases, more cold air is mixed away from the surface and brought to higher levels thus leading to lower temperatures in the atmosphere above the surface. They find this to be the case for solutions with exponential (concave up), or type I, θ profiles. As the wind speed increases even further, the air close to the surface begins to warm with increased wind speeds as now more warm air is able to reach the surface. *McNider et al.* found these solutions for concave down, or type II, θ profiles.

[71] In the current study, we also find the different behavior of the SBL for either increasing or decreasing the wind speed (see Figure 5). We find that for the wind regimes left of the T_{2m} minimum, T_{2m} *decreases* when the wind speed increases. The θ profiles (not shown here) then show a concave up, or more exponential shape (e.g., as in Figure 3c for the reference run and decreased mixing runs for a u_{geo} of 3 ms^{-1}). In these cases, when mixing or wind speed increases, the change in temperature for a fixed distance downward is larger than the change in temperature for a fixed distance upward. Therefore, a turbulent eddy centered at this given height will bring up cold air that more than compensates for the warm air brought down by the sinking part of the eddy. Hence, there will be a net cooling with enhanced mixing at this level. The opposite is true for a concave down θ profile which is found when wind speeds have increased sufficiently and are on the right of the T_{2m} minimum for the standard (1 K_Chm) and increased mixing runs (e.g., as in Figure 3c for the increased mixing runs). Then there will be net warming with enhanced mixing and wind speed.
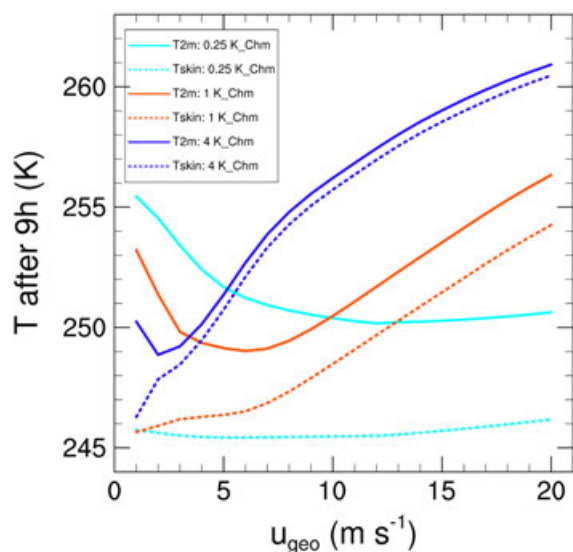

Figure 5. The modeled skin and 2 m temperature (K) after 9 h for different geostrophic wind speeds (u_{geo} (ms^{-1})) using varying turbulence intensities where mixing is adjusted in both boundary and surface layer. The solid lines refer to the 2 m temperatures and the dotted lines refer to the skin temperatures.

[72] Note that the difference in profile shape is not as profound for the decreased amount of mixing runs, where the θ profiles resemble a more exponential shape also on the right of the T_{2m} minimum, but they do show a weaker curvature for these wind speeds, which makes it easier for the mixing to overcome the temperature gradient close to the surface. Also when the wind speeds increase further, although the θ profile remains exponential, eddies with larger sizes can now reach the surface and bring warmer air from higher levels downward, which can compensate for the cold air that is brought upward from the surface. For the lower wind speeds, the eddies are relatively smaller so that the amount of downward-transported warm air is not sufficient to compensate for this effect.

[73] It is furthermore seen that the change in behavior shifts earlier (at lower u_{geo}) when the mixing is enhanced. Also, we see that for a more efficient mixing, the temperature difference between the surface and the 2 m level is smaller. In this way T_{2m} is indeed lower for higher amounts of mixing when u_{geo} is kept constant at a low value since the lower amount of mixing cannot mix away the large temperature gradient.

[74] The T_{skin} always increases when the amount of wind speed is increased for both the reference and the increased amount of mixing runs. For the 0.25 K_Chm runs we detect a very small decrease in T_{skin} when the wind speed is increased from 1 to 6 ms^{-1}. The reason for this is that due to the small sensible heat flux the cold air at the surface is not efficiently lifted and the mean SBL temperature remains relatively high. This results in an increase in $L\downarrow$ from the layers above the surface toward the surface which, when mixing or wind speeds decrease sufficiently, overcomes the radiative cooling, resulting in less cooling of the surface.

[75] For a $u_{geo} = 3$ ms^{-1} we detect a change from an exponentially shaped θ profile to a concave down-shaped profile when the amplification of mixing increases to 2.0 (see Figure 3c). Now the temperatures in the SBL decrease. When the amount of mixing increases further to 4.0 K_Chm, T_{2m} is still lower than T_{2m} for 1 K_Chm, but has increased compared to 2.0 K_Chm, indicating that there is more effective mixing with higher (and warmer) levels. For decreasing the amount of mixing for $u_{geo} = 8$ ms^{-1}, also the θ profile shifts from mixed to more exponentially shaped. The nonlinear effect is more profound for the K_Chm runs than the K runs. This is extended knowledge after *Bosveld et al.* [2012]. The decreased K runs, which have a similar altered mixing as in the study of *Bosveld et al.* [2012] over land, still have the normal amount of mixing in the surface layer and thus are more efficient in transporting cold air away from the surface and warmer air toward the surface so that this nonlinear effect is not as strongly visible.

[76] Note that this nonlinear behavior is also found from observations over sea ice and in the nocturnal SBL over land. *Lüpkes et al.* [2008] found that the minimum 10 m temperature observed during the SHEBA experiment in winter months is not observed for very calm conditions, but for a wind speed of ~4 ms^{-1}. Moreover, they found decreasing snow temperatures for increasing wind speeds up to ~4 ms^{-1} due to the reduced $L\downarrow$ from the colder air as was also found in our study. The nonlinearity was also detected by *Acevedo and Fitzjarrald* [2003] from measurements in the Albany region. They found that wind gusts below a certain

threshold (in their data $1.5 \, \mathrm{ms}^{-1}$) only mix the air downward to the colder ground, hence cooling the surface layer, while higher wind speeds cause mixing with higher levels as well and thus warming the surface layer. The existence of two different wind regimes with a threshold at wind speeds of $2–4 \, \mathrm{ms}^{-1}$ was furthermore reported by *Rinke et al.* [2012] from observations over the Antarctic.

6.4. Process Diagrams: Radiation Impacts

[77] Next we study which processes influence the temperature and radiative cooling at and near the surface. There is a tight coupling between the incoming and outgoing longwave radiation at the surface and the temperatures in the SBL and at the surface, respectively [*Bosveld et al.*, 2012]. Therefore, Figure 6 shows the process diagrams of the 2 m temperature and the net radiation (Q^*), both averaged over 9 h. Again we will first study the runs with a geostrophic wind speed of $8 \, \mathrm{ms}^{-1}$.

[78] The spread within the WRF SCM shows a strong correlation: when T_{2m} is high, a more negative Q^* can be found. This indicates that $L\uparrow$ dominates in the variation within the model intercomparison runs, since the extra $L\uparrow$ due to higher temperatures overcompensates the extra $L\downarrow$ resulting in a more negative Q^*.

[79] When studying the lines that are obtained with the sensitivity analysis, we find that the processes of increased mixing (K runs) and increased/decreased coupling are oriented in the same direction as the model intercomparison runs. For example when the amount of mixing or coupling is increased, a higher T_{2m} is found as well as a more negative Q^*. This is not the case when we look at the process of radiation. For increased $L\downarrow$ indeed not only a higher T_{2m} is found, but also a less negative Q^*, and the opposite occurs for a decreased amount of $L\downarrow$. Apparently for the radiation sensitivity, the change in $L\downarrow$ dominates over the change in $L\uparrow$. For both mixing runs, we again see the nonlinearity as was explained in the previous subsection. The spread within the model can mostly be explained by increasing the mixing strength (K runs) and increasing/decreasing the coupling strength, so that mixing and coupling appear to be complementary processes for these considered variables. Again the overall orientation of the K, λ, and q runs is similar as in *Bosveld et al.* [2012] without the nonlinear effect.

[80] Figure 6b gives the process diagram for $u_{\mathrm{geo}} = 3 \, \mathrm{ms}^{-1}$. Studying the lines representing coupling, we see a slight
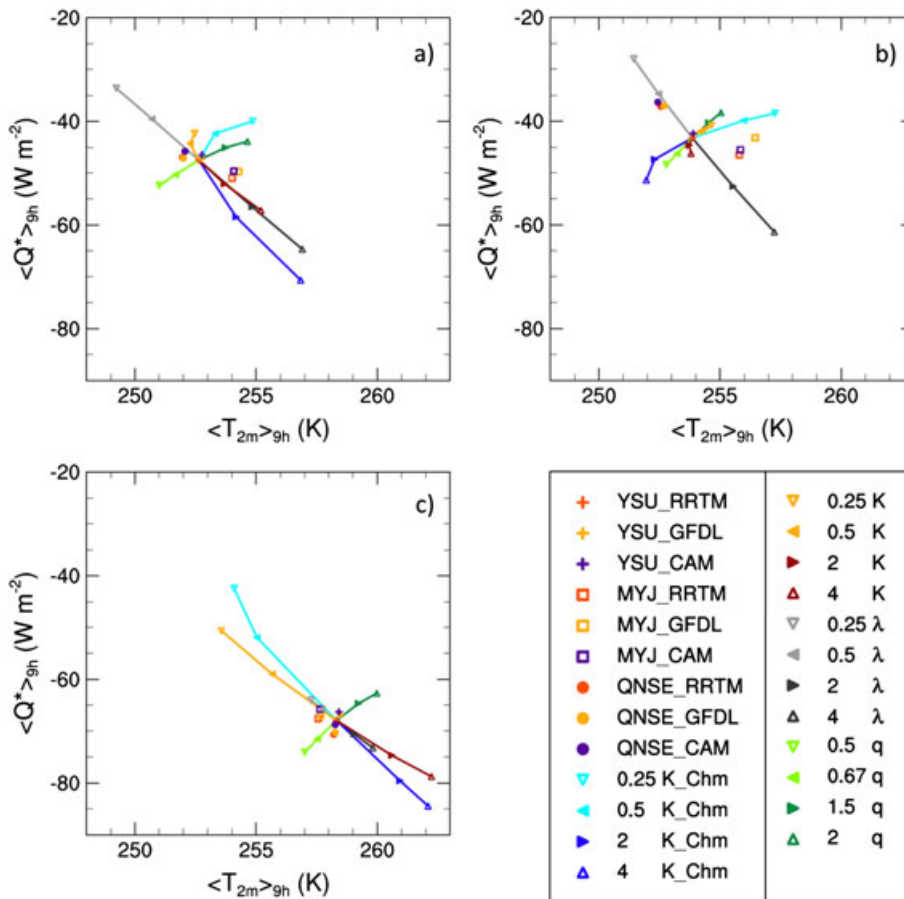

Figure 6. The 2 m temperature ($<T_{2m}>_{9h}$ (K)) versus the net radiation ($<Q^*>_{9h}$ (Wm^{-2})), both averaged over 9 h for a geostrophic wind speed of (a) $8 \, \mathrm{ms}^{-1}$, (b) $3 \, \mathrm{ms}^{-1}$, and (c) $20 \, \mathrm{ms}^{-1}$. K_Chm represents the eddy diffusivity and exchange coefficients and therefore the change in mixing in both boundary and surface layer, K represents the eddy diffusivity and therefore change in mixing in the boundary layer only, λ represents the ice conductivity and thus the coupling, and q represents the specific humidity profile and therefore the incoming longwave radiation. YSU-RRTM is the reference run.

change in orientation, the lines are more "steep," the change in T_{2m} is smaller for a similar change in $Q*$, however, they are not too different from the $8\,\mathrm{ms}^{-1}$ case. The orientation of the mixing lines however has changed orientation and direction, as was also the case in Figure 4b. The average T_{2m} decreases when the amount of mixing increases. As explained in the previous subsection, this phenomenon can occur when the BL is very weak and shallow and increased turbulence mixes cold air from the surface upward which is not sufficiently compensated by the downward transported warm air. $Q*$ does decrease with increased mixing. This is because $L\uparrow$ is determined by T_{skin}, and these do increase for increased mixing (see also Figure 5). For $u_{geo} = 3\,\mathrm{ms}^{-1}$, it is further observed that the model is more sensitive to mixing when also the amount of mixing in the surface layer is adjusted and not very sensitive to mixing only in the BL. The spread of the model intercomparison runs is now mostly found by a combination of increase in radiation, decrease in mixing, and a change in snow-surface coupling.

[81] The process diagram for T_{2m} and $Q*$ for $u_{geo} = 20\,\mathrm{ms}^{-1}$ (Figure 6c) again indicates that the effect of snow-surface coupling has decreased significantly, while the effect of mixing is relatively larger compared to the $8\,\mathrm{ms}^{-1}$, as was also observed in Figure 4. The model intercomparison runs show less spread than for the other wind speeds and cannot clearly be explained by one unique process modification.

6.5. Process Diagrams: Turbulent Mixing

[82] We continue with the process diagrams representing atmospheric mixing in showing the temperature difference between the lowest model level and the surface (ΔT), versus the sensible heat flux (H), both averaged over 9 h (Figure 7). H in the BL is determined by the eddy diffusivity for heat (K_h) and the potential temperature gradient ($\partial\theta/\partial z$) via

$$H = -\rho c_p K_h \frac{\partial\theta}{\partial z} \tag{3}$$

[83] Again we first focus on the case with $u_{geo} = 8\,\mathrm{ms}^{-1}$ in Figure 7a. When λ increases, more energy is added from the deeper ice layers to the atmosphere resulting in higher surface temperatures and hence a smaller ΔT, which consequently lowers the magnitude of H. The opposite occurs for decreasing the amount of coupling. If the amount of incoming radiation increases, the temperature difference
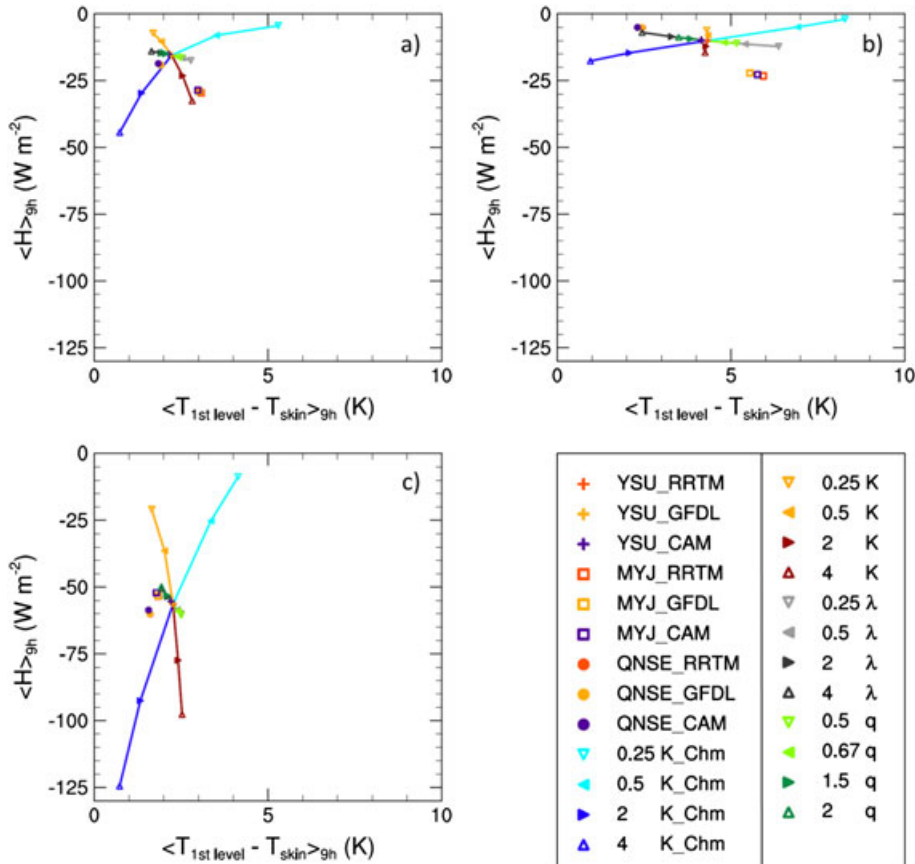

Figure 7. The temperature difference between the 2 m level and the surface ($< T_{\text{1st level}} - T_{skin} >_{9h}$ (K)) versus the sensible heat flux ($<H>_{9h}$ (Wm^{-2})), both averaged over 9 h for a geostrophic wind speed of (a) $8\,\mathrm{ms}^{-1}$, (b) $3\,\mathrm{ms}^{-1}$, and (c) $20\,\mathrm{ms}^{-1}$. K_Chm represents the eddy diffusivity and exchange coefficients and therefore the change in mixing in both boundary and surface layer, K represents the eddy diffusivity and therefore change in mixing in the boundary layer only, λ represents the ice conductivity and thus the coupling, and q represents the specific humidity profile and therefore the incoming longwave radiation. YSU-RRTM is the reference run.

becomes slightly smaller, and a similar orientation is found as for the coupling process.

[84] The amount of mixing in the K runs is adjusted by altering the eddy diffusivity coefficient in the BL scheme. The amount of mixing in the K_Chm runs is adjusted similarly, but includes an adjustment in the exchange coefficient in the land-surface model. When the amount of mixing in both the K_Chm runs and the K runs is increased, H increases due to the increased K_h. However, the orientation regarding ΔT differs, causing the orientation of the two mixing lines to be perpendicular. When the mixing increases, the temperature gradient decreases for the K_Chm runs, while an increase in temperature gradient is found for the K runs. The first behavior is what we would expect. When there is more mixing, the heat exchange between the surface and the atmosphere occurs more efficiently resulting in smaller temperature differences. That the temperature gradient increases with increased mixing for the K runs can be explained by the constant flux approach for which H in the surface layer equals H at the first model level. For the surface layer, H is determined with

$$H = -\rho c_p C_H u(\theta_1 - \theta_s) \qquad (4)$$

where C_H is the exchange coefficient for heat, u the wind speed and $\theta_1 - \theta_s$ represents the temperature difference between the first model level and the surface. In the constant flux approach, this equation should be equal to equation (3). When the amount of mixing in the surface layer is not adjusted, it follows from the equations that for an increase in K_h, there should be an increase in $\theta_1 - \theta_s$ and vice versa. In other words, an increase of K in the BL increases θ_1, but has little direct effect on θ_s, therefore ΔT increases and vice versa. This is indeed seen in Figure 7 for the K runs.

[85] When we compare the lines of the sensitivity analysis with the model intercomparison runs, we find that the orientation of the intercomparison runs can be explained by a combination of the K mixing process and coupling process. The model intercomparison runs are better represented by the K runs compared to the K_Chm. We expect this is due to the spread between the model intercomparison runs being dominated by the different BL schemes, and not the surface-layer schemes, since these are rather similar [Skamarock et al., 2008].

[86] Figure 7b gives the same process diagram for $u_{geo} = 3\,\text{ms}^{-1}$. Again, the orientation of the radiation and coupling lines is identical compared to those of a geostrophic wind speed of $8\,\text{ms}^{-1}$. The effect of change in coupling appears to be slightly more important than the effect of a change in radiation, since the 0.5 and 2.0 perturbations are equally oriented and the coupling line is longer. The length of the mixing line of the K_Chm runs is longer than the coupling line, although not in the orientation of the model intercomparison runs. The length of the mixing line for the K runs is very short as seen previously for this wind speed.

[87] Figure 7c presents the process diagram for $u_{geo} = 20\,\text{ms}^{-1}$. The orientation of the lines is comparable to the $8\,\text{ms}^{-1}$ case without the strong nonlinear effect, but the changes in H are now more profound, while the changes in ΔT at the surface are smaller for the coupling and radiation sensitivity runs. The latter can be explained by the already better mixed temperature profile. Again the line for snow-surface

coupling is rather short, a perturbation of 0.25 and 4.0 for coupling leads to similar results as perturbating radiation by 0.5 and 2.0, implying the insensitivity to snow-surface coupling in this wind regime. The radiation line points more in the direction of the orientation of the model intercomparison runs, but as for the other process diagrams, the largest sensitivity is found for the turbulent mixing process.

7. Rescaled Sensitivity Analyses

[88] In the previous section we perturbed each process by multiplying the coefficients with a prescribed amplification factor. However, multiplying for example the eddy diffusivity or the conductivity by such a factor may not necessarily have a similar impact on the atmospheric system in terms of energy and thus we would not compare the processes in a "fair" way. Therefore, we repeat the sensitivity analyses by varying the process strengths such that the change in surface net radiation (ΔQ^*) for the new run compared to the reference run is similar:

$$\Delta Q^* = \frac{1}{\Delta t}\left(\int Q_{SA}^* dt - \int Q_{ref}^* dt \right) \qquad (5)$$

[89] Here Q_{SA}^* is the net radiation for the sensitivity analysis run and Q_{ref}^* is the net radiation for the YSU-RRTM reference run. Δt is the total time difference (9 h) and dt represents the smaller time steps to calculate the integral. Table 3 gives an overview of the amount by which K_Chm, K, λ, and q were multiplied to achieve the desired ΔQ^* for $u_{geo} = 8\,\text{ms}^{-1}$. These prescribed ΔQ^*s are within the range of the ΔQ^*s that were found for the sensitivity analysis runs with the prescribed multiplication factors (see Table 2). We were unable to adjust the radiation process to a ΔQ^* of $7\,\text{Wm}^{-2}$ because the model did not reach this parameter range.

[90] Note that the choice of these multiplication factors might be timescale dependent, since ΔQ^* does not necessarily occur at the same rate for each physical process. Since we will

Table 3. Overview of the Changes in Net Radiation Over 9 h (ΔQ^*) for $u_{geo} = 8\,\text{ms}^{-1}$ and the Factor by Which Both the Eddy Diffusivity and Exchange Coefficient (K_Chm), Only the Eddy Diffusivity (K), the Ice Conductivity (λ), and the Initial Specific Humidity Profile (q) Are Multiplied to Obtain This Net Radiation Change

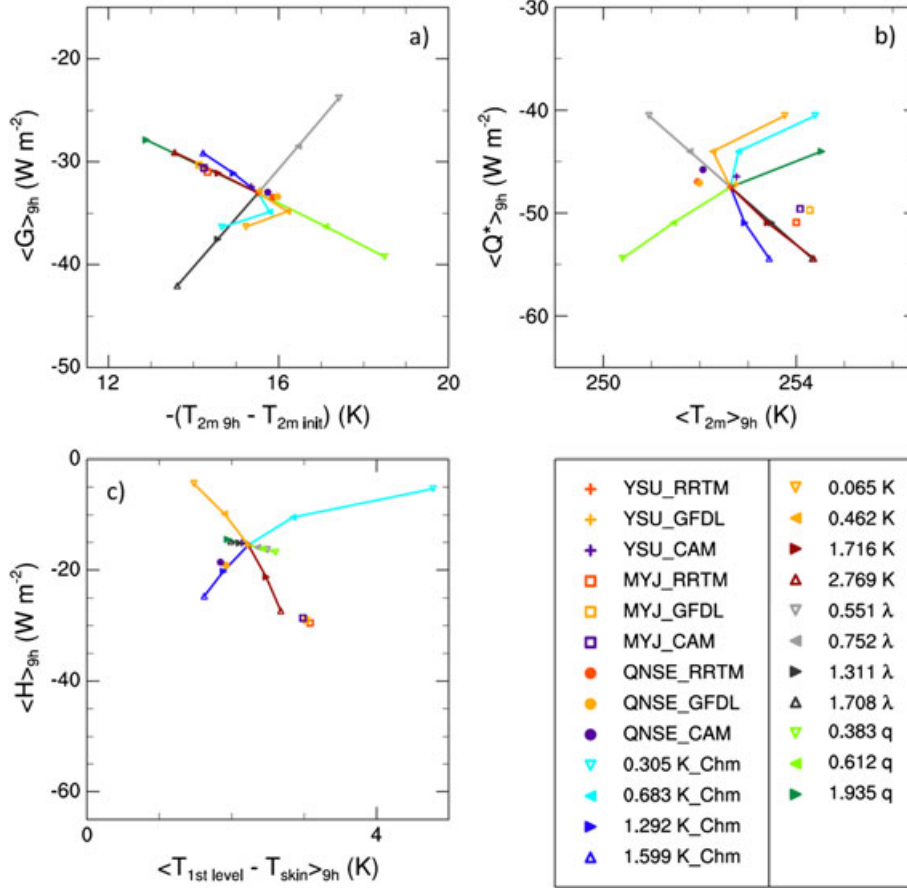| Parameter	ΔQ^* (Wm^{-2})	Multiplication Factor
K_Chm	7	0.305
	3.5	0.683
	−3.5	1.292
	−7	1.599
K	7	0.065
	3.5	0.462
	−3.5	1.716
	−7	2.769
λ	7	0.551
	3.5	0.752
	−3.5	1.311
	−7	1.708
q	3.5	1.935
	−3.5	0.612
	−7	0.383

Figure 8. Process diagrams for a geostrophic wind speed of $8\,\mathrm{ms}^{-1}$ of (a) the cooling of the 2 m temperature $(-(T_{2m9h} - T_{2minit})\,(\mathrm{K}))$ over the 9 h run versus the soil heat flux $(<G>_{9h}\,(\mathrm{Wm}^{-2}))$ averaged over 9 h, (b) the 2 m temperature $(<T_{2m}>_{9h}\,(\mathrm{K}))$ versus the net radiation $(<Q^*>_{9h}\,(\mathrm{Wm}^{-2}))$, both averaged over 9 h, and (c) the temperature difference between the 2 m level and the surface $(<T_{1stlevel} - T_{skin}>_{9h}\,(\mathrm{K}))$ versus the sensible heat flux $(<H>_{9h}\,(\mathrm{Wm}^{-2}))$, both averaged over 9 h. In all cases ΔQ^* is kept similar, i.e., $\Delta Q^* = 7$, 3.5, -3.5, and $-7\,\mathrm{Wm}^{-2}$. YSU-RRTM is the reference run.

examine ΔQ^* over the entire 9 h run, it is justified to adjust the parameters such that the surface energy change at 9 h is similar. Figure 8 depicts the same process diagrams as discussed in the previous section, for $u_{geo} = 8\,\mathrm{ms}^{-1}$. We adjusted the axis, but kept them in the same proportion as Figures 4, 6, and 7 for better comparison.

[91] When we compare Figures 8a–8c with Figures 4, 6, and 7 a, in general we see a similar orientation, but a decrease in line length for the K_Chm and λ runs and for the increased K runs. The line length of reduced K runs has increased due to the stronger perturbation factor that was applied to achieve a ΔQ^* of $7\,\mathrm{Wm}^{-2}$ than the multiplication factors as applied in the previous section. These differences with the previous Figures indicate the importance of the choice for the multiplication factors of the parameters.

[92] To get a ΔQ^* of $3.5\,\mathrm{Wm}^{-2}$ for $u_{geo} = 3\,\mathrm{ms}^{-1}$, the K_Chm run had to be multiplied by 0.488, the K run by 0.103, the λ run by 0.763, and the q run by 1.628. These findings indicate that for low wind speed the model is not that sensitive to mixing, and especially to mixing in the BL scheme only, while being more sensitive to coupling and radiation. This is supported by the ΔQ^*s that were found when the prescribed amplification factors were applied in the previous section (see Table 2). For a u_{geo} of $3\,\mathrm{ms}^{-1}$ we

find smaller changes in ΔQ^* for the mixing runs, especially the K runs, and larger changes for the coupling runs compared to the $u_{geo} = 8\,\mathrm{ms}^{-1}$ runs. The radiation runs only show minor differences between the ΔQ^*.

[93] For $u_{geo} = 20\,\mathrm{ms}^{-1}$, we had to multiply K_Chm by 0.861, K by 0.756, λ by 0.312, and q by 1.542 to obtain a ΔQ^* of $3.5\,\mathrm{Wm}^{-2}$. When we compare ΔQ^* for $u_{geo} = 20\,\mathrm{ms}^{-1}$ with $8\,\mathrm{ms}^{-1}$ while keeping the multiplication factor for each process equal in Table 2, we see stronger changes for the mixing runs and smaller changes for the coupling runs. The changes are stronger when the amount of mixing is decreased, since the signal is mixed over a shallower boundary layer. The radiation runs do show a somewhat larger difference in ΔQ^* as well.

8. Conclusions and Discussion

[94] This study focuses on identifying the dominant governing processes in the Arctic stable boundary layer for different wind regimes. We consider three physical processes, i.e., snow-surface coupling, radiation, and turbulent mixing. First we perform a 1D model intercomparison within the WRF framework, by varying the boundary layer and longwave radiation schemes for the GABLS1 case

[Beare et al., 2006; Cuxart et al., 2006]. Hence, we quantify the spread between the different model schemes. To explain this spread, we perform a sensitivity analysis for the three governing processes.

[95] Overall we notice a shift in significance of the different processes for varying wind regimes. In situations with high wind speeds, model output is most sensitive to turbulent mixing, while the effects of radiation and especially the snow-surface coupling are small (as one could anticipate), as seen from the strongest change in potential temperature and wind speed profile, and from the relatively long sensitivity lines in the process diagrams [Bosveld et al., 2012] for the mixing process.

[96] Considering situations with low wind speeds, we reveal that the model is most sensitive to snow-surface coupling and radiation in the SBL structure and evolution. Then, the impact of turbulent mixing is minor except when the mixing strength is also adjusted in the surface layer. This stresses the significance of consistently linking the surface layer with the boundary layer.

[97] For the cases with a geostrophic wind speed of 8 and $20 \, \mathrm{ms}^{-1}$, we find a relatively mixed boundary layer profile topped by a strong inversion, though when we decrease the amount of mixing by 0.25 and 0.5 (for $8 \, \mathrm{ms}^{-1}$) and 0.25 (for $20 \, \mathrm{ms}^{-1}$), this becomes more exponential. For a low wind speed of $3 \, \mathrm{ms}^{-1}$, a more exponential profile shape for the reference run is found, although this becomes better mixed for a higher turbulent mixing strength. Thus, even though choosing a different mixing parameter may not significantly affect the surface variables, it does strongly influence the vertical profiles and thus possibly other variables away from the surface. Therefore, it is recommended that when evaluating and optimizing a model, the vertical structure should be considered as well. If the model is optimized for 2 m temperatures, as often occurs in operational studies, it is likely that the model results deviate aloft.

[98] Furthermore, an intriguing nonlinear behavior regarding the effects on temperature just above the surface is found, as was also seen in observations [Acevedo and Fitzjarrald, 2003; Lüpkes et al., 2008; Rinke et al., 2012]. The 2 m temperature decreases for increased mixing strength and vice versa. The skin temperature, however, does increase for increased mixing strength and vice versa. This suggests that mixing occurs only in a shallow layer close to the surface and cold air that is mixed upward is not fully compensated by downward mixed warm air. These findings do have an implication for the understanding of the Arctic climate, since apparently the behavior at the 2 m level is not straightforward, while the 2 m temperature is often used in research.

[99] Moreover, this "counterintuitive" behavior was found for low wind speeds with exponential (or concave up) potential temperature shapes [McNider et al., 2012], when relatively more cold air is mixed toward the 2 m level than warm air is transported downward. For higher wind speeds, we find better mixed (or concave down) potential temperature profiles, where there is a more efficient redistribution of heat and 2 m temperatures increase with increased wind speeds. Keeping the wind speed constant, this nonlinear behavior can also occur for better mixed boundary layer profiles when the mixing strength is decreased and the temperature inversion at the surface increases greatly.

[100] The process diagrams indicate that some process sensitivity lines can overlap, which implies that variations due to these processes can compensate each other. This further implies that errors in either process parameterization can remain hidden by the parameterization of the other process, keeping it unclear if the model is less physically realistic. Unfortunately, the two overlapping processes are not the same for various sets of variables. Hence, in order to proceed in model development, processes should not be studied in isolation. This requires coordination of many different types of measurements which poses a challenge for observationalists.

[101] This study explored the relative significance of the governing physical processes for a cooling Arctic SBL compared to each other under different wind regimes. Moreover, future work is calling for observational confirmation of the current work. In this way, we would know how to improve the model. However, this study is for an idealized set-up and we were unable to directly compare our model results with observations.

[102] Overall, the representation of small-scale processes in the Arctic SBL remains challenging. Although there is not one single process absolutely governing the evolution and structure of the SBL, we were able to indicate a shift in their relative significance for changing wind regimes and we confirmed the nonlinear behavior of turbulent mixing regarding the temperatures close to the surface for frequently occurring wind speeds. Therefore, in regimes with high wind speeds we think it is worthwhile to focus on improving the turbulent mixing schemes, while for low wind speed regimes better investments can be made in land-surface and radiation schemes. However, due to the nonlinearity effects that we detected, choosing the amount turbulent mixing should be done wisely, not only for proper forecasting of temperatures close to the surface but also for the entire atmospheric profile and hence transports aloft.

References

Acevedo, O. C., and D. R. Fitzjarrald (2003), In the core of the night—Effects of intermittent mixing on a horizontally heterogeneous surface, *Boundary Layer Meteorol.*, *106*, 1–33, doi:10.1023/A:1020824109575.

Alexeev, V. A., P. L. Langen, and J. R. Bates (2005), Polar amplification of surface warming on an aqua planet in "ghost forcing" experiments without sea ice feedbacks, *Clim. Dyn.*, *24*, 655–666, doi:10.1007/s00382-005-0018-3.

André, J. C., and L. Mahrt (1982), The nocturnal surface inversion and influence of clear-air radiative cooling, *J. Atmos. Sci.*, *39*, 864–878, doi:10.1175/1520-0469(1982)039<0864:TNSIAI>2.0.CO;2.

Andreas, E. L. (1987) A theory for the scalar roughness and the scalar transfer coefficients over snow and sea ice, *Boundary Layer Meteorol.*, *38*, 159–184, doi:10.1007/BF00121562.

Andreas, E. L., P. O. G. Persson, R. E. Jordan, T. W. Horst, P. S. Guest, A. A. Grachev, and C.W. Fairall (2010), Parameterizing turbulent exchange over sea ice in winter, *J. Hydrometeorol.*, *11*, 87–104, doi:10.1175/2009JHM1102.1.

Arctic Climate Impact Assessment (ACIA) (2005), Arctic Climate Impact Assessment, 1042 pp., Cambridge Univ. Press, Cambridge, U.K.

Atlaskin, E., and T. Vihma (2012), Evaluation of NWP results for wintertime nocturnal boundary-layer temperatures over Europe and Finland, *Q. J. R. Meteorol. Soc.*, doi:10.1002/qj.1885.

Beare, R. J., et al. (2006), An intercomparison of large-eddy simulations of the stable boundary layer, *Boundary Layer Meteorol.*, *118*, 247–272, doi:10.1007/s10546-004-2820-6.

Beljaars, A. C. M., and A. A. M. Holtslag (1991), Flux parameterization over land surfaces for atmospheric models, *J. Appl. Meteorol.*, *30*, 327–341, doi:10.1175/1520-0450(1991)030<0327:FPOLSF>2.0.CO;2.

Beljaars, A. C. M., and P. Viterbo (1998), Role of the boundary layer in a numerical weather prediction model, in Clear and Cloudy Boundary Layers, pp. 287-304, A.A.M. Holtslag and P.G. Duynkerke Eds, Royal Netherlands Academy of Arts and Sciences, Amsterdam.

Bintanja, R., R. G. Graversen, and W. Hazeleger (2011a), Arctic winter warming amplified by the thermal inversion and consequent low infrared cooling to space, *Nat. Geosci.*, *4*, 758–761, doi:10.1038/NGEO1285.

Bintanja, R., E. C. van der Linden, and W. Hazeleger (2011b), Boundary layer stability and Arctic climate change: A feedback study using EC-Earth, *Clim. Dyn.*, doi:10.1007/s00382-011-1272-1.

Boé, J., A. Hall, and X. Qu (2009), Current GCMs' unrealistic negative feedback in the Arctic, *J. Clim.*, *22*, 4682–4695, doi:10.1175/2009JCLI2885.1.

Bony, S., et al. (2006), Review article: How well do we understand and evaluate climate change feedback processes?, *J. Clim.*, *19*, 3445–3482, doi:10.1175/JCLI3819.1.

Bosveld, F. C., P. Baas, G. J. Steeneveld, and A. A. M. Holtslag (2012), GABLS3 SCM intercomparison and evaluation: What did we learn?, *Proceedings of the Workshop on Diurnal cycles and the stable boundary layer, 7-10 November, 2011*, pp. 91-102, Co-sponsored by ECMWF and WCRP, Reading, U.K., http://www.ecmwf.int/publications/library/do/references/list/201111

Chen, F., and J. Dudhia (2001), Coupling an advanced land surface-hydrology model with the Penn State-NCAR MM5 modelling system. Part I: Model implementation and sensitivity. *Mon. Weather Rev.*, *129*, 569–585, doi:10.1175/1520-0493(2001)129<0569:CAALSH>2.0.CO;2.

Claffey, K. J., E. L. Andreas, Perovich D. K., Fairall C. W., Guest P. S., and P.O.G. Persson (1999), Surface temperature measurements at SHEBA, *Preprints, Fifth Conference on Polar Meteorology and Oceanography*, pp. 327–332, American Meteorological Society, Dallas, Texas.

Collins, W. D., et al. (2004), Description of the NCAR Community Atmosphere Model (CAM 3.0), NCAR Technical Note, 226 pp., Climate and Global Dynamics Division, National Center for Atmospheric Research (NCAR), Boulder, Colorado (http://www.cesm.ucar.edu/models/atm-cam/docs/description/description.pdf).

Comiso, J. C., C. L. Parkinson, R. Gertsen, and L. Stock (2008), Accelerated decline in the Arctic sea ice cover. *Geophys. Res. Lett.*, *35*, L01703, doi:10.1029/2007GL031972.

Curry, J. A., Schramm J. L., and E. E. Ebert (1995), Sea ice-albedo climate feedback mechanism. *J. Clim.*, *8*, 240–247, doi:10.1175/1520-0442(1995)008<SIACFM>2.0.CO;2.

Cuxart, J., et al. (2006), Single-column model intercomparison for a stably stratified atmospheric boundary layer, *Boundary Layer Meteorol.*, *118*, 273–303, doi:10.1007/s10546-005-3780-1.

Delage, Y. (1997), Parameterising sub-grid scale vertical transport in atmospheric models under statically stable conditions, *Boundary Layer Meteorol.*, *82*, 23–48, doi:10.1023/A:1000132524077.

Derbyshire, S. H. (1999), Boundary-layer decoupling over cold surfaces as a physical boundary instability, *Boundary Layer Meteorol.*, *90*, 297–325, doi:10.1023/A:1001710014316.

Domine, F., J. C. Gallet, J. Bock, and S. Morin (2012), Structure, specific surface area and thermal conductivity of the snowpack around Barrow, Alaska, *J. Geophys. Res.*, *117* D00R14, doi:10.1029/2011JD016647.

Dutra, E., C. Schär, P. Viterbo, and P. M. A. Miranda (2011), Land-atmosphere coupling associated with snow cover, *Geophys. Res. Lett.*, *38*, L15707, doi:10.1029/2011GL048435.

Duynkerke, P. G. (1991), Radiation fog: A comparison of model simulation with detailed observations, *Mon. Weather Rev.*, *119*, 324–341, doi:10.1175/1520-0493(1991)119<0324:RFACOM>2.0.CO;2.

Edwards, J. M. (2009), Radiative processes in the stable boundary layer: Part I. *Radiative Aspects, Boundary Layer Meteorol.*, *131*, 105–126, doi:10.1007/s10546-009-9364-8.

Ek, M. B., Mitchell K. E., Lin Y., Rogers E., Grunmann P., Koren V., Gayno G., and J. D. Tarpley (2003), Implementation of Noah land surface model advances in the National Centers for Environmental Prediction operational mesoscale Eta model, *J. Geophys. Res.*, *108*(D22), 8851, doi:10.1029/2002JD003296.

European Centre for Medium-Range Weather Forecasts (ECMWF) (2009), IFS Documentation Cy33r1, operational implementation 3 June 2008, Part IV: Physical processes, 162 pp., Reading, U.K. (http://www.ecmwf.int/research/ifsdocs/CY33r1/PHYSICS/IFSPart4.pdf).

European Centre for Medium-Range Weather Forecasts (ECMWF) (2012), IFS Documentation Cy37r2, operational implementation 18 May 2011, Part IV: Physical Processes, 174 pp., Reading, U.K. (http://www.ecmwf.int/research/ifsdocs/CY37r2/IFSPart4.pdf).

Garratt, J. R., and R. A. Brost (1981), Radiative cooling effects within and above the nocturnal boundary layer, *J. Atmos. Sci.*, *38*, 2730–2746, doi:10.1175/1520-0469(1981)038<2730:RCEWAA>2.0.CO;2.

Gouttevin, I., M. Menegoz, F. Dominé, G. Krinner, C. Koven, P. Ciais, C. Tarnocai, and J. Boike (2012), How the insulating properties of snow affect soil carbon distribution in the continental pan-Arctic area, *J. Geophys. Res.*, *117* G02020, doi:10.1029/2011JG001916.

Grachev, A. A., Fairall C. W., Persson P. O. G., Andreas E. L., and P. S. Guest (2005), Stable boundary-layer scaling regimes: The SHEBA data, *Boundary Layer Meteorol.*, *116*, 201–235, doi:10.1007/s10546-004-2729-0.

Grachev, A. A., E. L. Andreas, C. W. Fairall, P. S. Guest, and P. O. G. Persson (2007), SHEBA flux-profile relationships in the stable atmospheric boundary layer, *Boundary Layer Meteorol.*, *124*, 315–333, doi:10.1007/s10546-007-9177-6.

Graversen, R. G., T. Mauritsen, M. Tjernström, E. Källén, and G. Svensson (2008), Vertical structure of recent Arctic warming, *Nature*, *451*, 53–56, doi:10.1038/nature06502.

Graversen, R. G., and M. Wang (2009), Polar amplification in a coupled climate model with locked albedo, *Clim. Dyn.*, *33*, 629–643, doi:10.1007/s00382-009-0535-6.

Hanna, S. R., and R. Yang (2001), Evaluations of mesoscale models' simulations of near-surface winds, temperature gradients, and mixing depths, *J. Appl. Meteorol.*, *40*, 1095–1104, doi:10.1175/1520-0450(2001)040<1095:EOMMSO>2.0.CO;2.

Hoch, S. W., P. Calanca, R. Philipona, and A. Ohmura (2007), Year-round observation of longwave radiative flux divergence in Greenland, *J. Appl. Meteorol. Climatol.*, *46*, 1469-1479, doi:10.1175/JAM2542.1.

Holland, M. M., and C. M. Bitz (2003), Polar amplification of climate change in coupled models, *Clim. Dyn.*, *21*, 221–232, doi:10.1007/s00382-003-0332-6.

Holtslag, A. A. M., and H. A. R. de Bruin (1988), Applied modelling of the nighttime surface energy balance over land, *J. Appl. Meteorol.*, *27*, 689–704, doi: 10.1175/1520-0450(1988)027<0689:AMOTNS>2.0.CO;2.

Holtslag, A. A. M., and B. A. Boville (1993), Local versus nonlocal boundary-layer diffusion in a global climate model, *J. Clim.*, *6*, 1825–1842, doi: 101175/1520-0442(1993)006<1825LVNBLD>2.0.CO;2.

Holtslag, A. A. M. (2006), GEWEX atmospheric boundary-layer study (GABLS) on stable boundary layers, *Boundary Layer Meteorol.*, *118*, 243–246, doi: 10.1007/s10546-005-9008-6.

Holtslag, A. A. M., G. J. Steeneveld, and B. J. H. van de Wiel (2007), Role of land-surface temperature feedback on model performance for the stable boundary layer, *Boundary Layer Meteorol.*, *125*, 361–376, doi:10.1007/s10546-007-9214-5.

Holtslag, A. A. M., G. Svensson, S. Basu, B. Beare, F. C. Bosveld, and J. Cuxart (2012), Overview of the GEWEX Atmospheric Boundary Layer Study (GABLS), *Proceedings of the Workshop on Diurnal Cycles and the Stable Boundary Layer, 7-10 November 2011*, pp. 11-23, Co-sponsored by ECMWF and WCRP, Reading, U.K., http://www.ecmwf.int/publications/library/do/references/list/201111

Hong, S. Y., Y. Noh, and J. Dudhia (2006), A new vertical diffusion package with an explicit treatment of entrainment processes, *Mon. Weather Rev.*, *134*, 2318–2341, doi:10.1175/MWR3199.1.

Hong, S. Y., and S. W. Kim (2008). Stable boundary layer mixing in a vertical diffusion scheme. *18th Symposium on Boundary Layers and Turbulence*, 16B.2, Stockholm, Sweden, 9-13 June 2008, Amer. Meteorol. Soc., Boston.

Hu, X. M., J. W. Nielsen-Gammon, and F. Zhang (2010), Evaluation of three planetary boundary layer schemes in the WRF model, *J. Appl. Meteorol. Climatol.*, *49*, 1831–1844, doi:10.1175/2010JAMC2432.1.

Hunke, H., and W. Meier (2012), Polar boundary layer processes: Important factors for investigating biogeochemistry and climate, *Eos Trans. AGU*, *93*, (44), 441, doi:10.1029/2012EO440008.

Huwald, H., L. B. Tremblay, and H. Blatter (2005), Reconciling different observational data sets from Surface Heat Budget of the Arctic Ocean (SHEBA) for model validation purposes, *J. Geophys. Res.*, *110*, C05009, doi:10.1029/2003JC002221.

Iacono, M. J., E. J. Mlawer, S. A. Clough, and J. J. Morcrette (2000), Impact of an improved longwave radiation model, RRTM, on the energy budget and thermodynamic properties of the NCAR community climate model, CCM3, *J. Geophys. Res.*, *105D11*, 14873–14890, doi:10.1029/2000JD900091.

Inoue, J., J. Liu, J. O. Pinto, and J. A. Curry (2006), Intercomparison of Arctic regional climate models: Modeling clouds and radiation for SHEBA in May 1998, *J. Clim.*, *19*, 4167–4178, doi:10.1175/JCLI3854.1.

Intrieri, J. M., C. W. Fairall, M. D. Shupe, P. O. G. Persson, E. L. Andreas, P. S. Guest, and R. E. Moritz (2002), An annual cycle of Arctic surface

cloud forcing at SHEBA, *J. Geophys. Res.*, *107* No. C10, 8039, doi:10.1029/2000JC000439.

Jiménez, P. A., J. Dudhia, J. Fidel González-Rouco, J. Navarro, J. P. Montávez, and E. García-Bustamante, (2011), A revised scheme for the WRF surface layer formulation, *Mon. Weather Rev.*, *140*, 898–918, doi:10.1175/MWR-D-11-00056.1.

Johannessen, O. M., et al. (2004), Arctic climate change: Observed and modelled temperature and sea-ice variability, *Tellus*, *56A*, 328–341, doi:10.1111/j.1600-0870.2004.00060.x.

Kondo, J., and H. Yamazawa (1986), Measurement of snow surface emissivity, *Boundary Layer Meteorol.*, *34*, 415–416, doi:10.1007/BF00120992.

Kosovic, B., and J. A. Curry (2000), A large eddy simulation study of a quasi-steady, stably stratified atmospheric boundary layer, *J. Atmos. Sci.*, *57*, 1052–1068, doi:10.1175/1520-0469(2000)057<1052:ALESSO>2.0.CO;2.

Lüpkes, C., T. Vihma, G. Birnbaum, and U. Wacker (2008), Influence of leads in sea ice on the temperature of the atmospheric boundary layer during polar night, *Geophys. Res. Lett.*, *35*, L03805, doi:10.1029/2007GL032461.

Mahrt, L., J. Sun, W. Blumen, T. Delany, and S. Oncley (1998), Nocturnal boundary-layer regimes, *Boundary Layer Meteorol.*, *88*, 255–278, doi:10.1023/A:1001171313493.

Mahrt, L. (1999), Stratified atmospheric boundary layers, *Boundary Layer Meteorol.*, *90*, 375–396, doi:10.1023/A:1001765727956.

Mäkiranta, E., T. Vihma, A. Sjöblom, and E. M. Tastula (2011), Observations and modelling of the atmospheric boundary layer over sea-ice in a Svalbard fjord, *Boundary Layer Meteorol.*, *140*, 105–123, doi:10.1007/s10546-011-9609-1.

Mauritsen, T., G. Svensson, S. S. Zilitinkevich, I. Esau, L. Enger, and B. Grisogono (2007), A total turbulent energy closure model for neutrally and stably stratified atmospheric boundary layers, *J. Atmos. Sci.*, *64*, 4113–4126, doi:10.1175/2007JAS2294.1.

McNider, R. T., G. J. Steeneveld, A. A. M. Holtslag, R. A. Pielke Sr., S. Mackaro, A. Pour-Biazar, J. Walters, U. Nair, and J. Christy (2012), Response and sensitivity of the nocturnal boundary layer over land to added longwave radiative forcing, *J. Geophys. Res.*, doi:10.1029/2012JD017578.

Mellor, G. L., and T. Yamada (1982), Development of a turbulence closure model for geophysical fluid problems, *Rev. Geophys. Space Phys.*, *20*, No. (4), 851–875, doi:10.1029/RG020i004p00851.

Mlawer, E. J., S. J. Taubman, P. D. Brown, M. J. Iacono, and S. A. Clough (1997), Radiative transfer for inhomogeneous atmospheres: RRTM, a validated correlated-k model for the longwave, *J. Geophys. Res.*, *102D14*, 16663–16682, doi:10.1029/97JD00237.

Morcrette, J. J., E. J. Mlawer, M. J. Iacono, and S. A. Clough (2001), Impact of the radiation-transfer scheme RRTM in the ECMWF forecasting system. *ECMWF Newsletter*, pp. 2-9, No. 91, Reading, U.K.

Persson, P. O. G., C. W. Fairall, E. L. Andreas, P. S. Guest, and D. K. Perovich (2002), Measurements near the Atmospheric Surface Flux Group tower at SHEBA: Near-surface conditions and surface energy budget, *J. Geophys. Res.*, *107* No. (C10), 8045, doi:10.1029/2000JC000705.

Rinke, A., et al. (2006), Evaluation of an ensemble of Arctic regional climate models: Spatiotemporal fields during the SHEBA year, *Clim. Dyn.*, *26*, 459–472, doi:10.1007/s00382-005-0095-3.

Rinke, A., Y. Ma, L. Bian, Y. Xin, K. Dethloff, P. O. G. Persson, C. Lüpkes, and C. Xiao (2012), Evaluation of atmospheric boundary-layer surface process relationships in a regional climate model along an East Antarctic traverse, *J. Geophys. Res.*, *117*, D09121, doi:10.1029/2011JD016441.

Rodgers, C. D. (1967), The use of emissivity in atmospheric radiation calculation, *Q. J. R. Meteorol. Soc.*, *93*, 43–54, doi:10.1002/qj.49709339504.

Roeckner, E., et al. (2003), Report No. 349: The atmospheric general circulation model ECHAM5, *Part 1, Model Description*. Max Planck Institute for Meteorology, 140 pp., Hamburg, Germany (http://www.mpimet.mpg.de/fileadmin/publikationen/Reports/max_scirep_349.pdf).

Salmond, J. A., and I. G. McKendry (2005), A review of turbulence in the very stable nocturnal boundary layer and its implications for air quality, *Prog. Phys. Geogr.*, *29*, 171–188, doi:10.1191/0309133305pp442ra.

Schröder, D., T. Vihma, A. Kerber, and B. Brümmer (2003), On the parameterization of turbulent surface fluxes over heterogeneous sea ice surfaces, *J. Geophys. Res.*, *108* No. C6, 3195, doi:10.1029/2002JC001385.

Serreze, M. C., R. G. Barry, and J. E. Walsh (1995), Atmospheric water vapor characteristics at 70°N, *J. Clim.*, *8*, 719–731, doi:10.1175/1520-0442(1995)008<0719:AWVCA>2.0.CO;2.

Serreze, M. C., and J. A. Francis (2006), The Arctic amplification debate, *Clim. Change*, *76*, 241–264, doi:10.1007/s10584-005-9017-y.

Serreze, M. C., A. P. Barrett, and J. J. Cassano (2011), Circulation and surface controls on the lower tropospheric air temperature field of the Arctic, *J. Geophys. Res.*, *116*, D07104, doi:10.1029/2010JD015127.

Shin, H. H., and S. Y. Hong (2011), Intercomparison of planetary boundary-layer parameterizations in the WRF model for a single day from CAES-99, *Boundary Layer Meteorol.*, *139*, 261–281, doi:10.1007/s10546-010-9583-z.

Shupe, M. D., and J. M. Intrieri (2004), Cloud radiative forcing of the Arctic surface: The influence of cloud properties, surface albedo, and solar zenith angle, *J. Clim.*, *17*, 616–628, doi:10.1175/1520-0442(2004)017<0616:CRFOTA>2.0.CO;2.

Skamarock, W. C., J. B. Klemp, J. Dudhia, D. O. Gill, D. M. Barker, M. G. Duda, X. Y. Huang, W. Wang, and J. G. Powers (2008), A Description of the Advanced Research WRF Version 3, Mesoscale and Microscale Meteorology Division, National Center for Atmospheric Research (NCAR), 113 pp., Boulder, Colorado, U.S.A. (http://www.mmm.ucar.edu/wrf/users/docs/arw_v3.pdf).

Steeneveld, G. J., B. J. H. van de Wiel, and A. A. M. Holtslag (2006a), Modelling the Arctic nocturnal stable boundary layer and its coupling to the surface, *Boundary Layer Meteorol.*, *118*, 357–378, doi:10.1007/s10546-005-7771-z.

Steeneveld, G. J., B. J. H. van de Wiel, and A. A. M. Holtslag (2006b), Modeling the evolution of the atmospheric boundary layer coupled to the land surface for three contrasting nights in CASES-99, *J. Atmos. Sci.*, *63*, 920–935, doi:10.1175/JAS3654.1.

Stensrud, D. J. (2007), Parameterization Schemes: Keys to Understanding Numerical Weather Prediction Models, 459 pp., Cambridge University Press, Cambridge.

Stramler, K., A. D. Del Genio, and W. B. Rossow (2011), Synoptically driven Arctic winter states, *J. Clim.*, *24*, 1747–1762, doi:10.1175/2010JCLI3817.1.

Sturm, M., D. K. Perovich, and J. Holmgren (2002), Thermal conductivity and heat transfer through the snow on the ice of the Beaufort Sea, *J. Geophys. Res.*, *107*, No. (0), doi:10.1029/2000JC000409.

Sukoriansky, S., B. Galperin, and V. Perov (2006), A quasi-normal scale elimination model of turbulence and its application to stably stratified flows, *Nonlinear Processes Geophys.*, *13*, 9–22, doi:10.5194/npg-13-9-2006.

Sukoriansky, S. (2008), Implementation of the Quasi-Normal Scale Elimination (QNSE) model of stably stratified turbulence in WRF, *Report on WRF-DTC Visit*, Developmental Testbed Center, 8 pp., http://www.dtcenter.org/visitors/reports_07/Sukoriansky_report.pdf.

Svensson, G., and A. A. M. Holtslag (2009), Analysis of model results for the turning of the wind and related momentum fluxes in the stable boundary layer, *Boundary Layer Meteorol.*, *132*, 261–277. doi:10.1007/s10546-009-9395-1.

Svensson, G., and J. Karlsson (2011), On the Arctic wintertime climate in Global Climate Models, *J. Clim.*, *24*, 5757–5771, doi:10.1175/2011JCLI4012.1.

Tastula, E. M., and T. Vihma (2011), WRF model experiments on the Antarctic atmosphere in winter, *Mon. Weather Rev.*, *139*, 1279–1291, doi:10.1175/2010MWR3478.1.

Tjemkes, S. A., and P. G. Duynkerke (1989), The nocturnal boundary layer: Model calculations compared with observations, *J. Appl. Meteorol.*, *28*, 161–175, doi:10.1175/1520-0450(1989)028<0161:TNBLMC>2.0.CO;2.

Tjernström, M., et al. (2005), Modelling the Arctic boundary layer: An evaluation of six ARCMIP regional-scale models using data from the SHEBA project, *Boundary Layer Meteorol.*, *117*, 337–381, doi:10.1007/s10546-004-7954-z.

Tjernström, M., and R. G. Graversen (2009), The vertical structure of the lower Arctic troposphere analysed from observations and the ERA-40 reanalysis, *Q. J. R. Meteorol. Soc.*, *135*, 431443, doi:10.1002/qj.380.

Troen, I. B., and L. Mahrt (1986), A simple model of the atmospheric boundary layer; sensitivity to surface evaporation, *Boundary Layer Meteorol.*, *37*, 129–148, doi:10.1007/BF00122760.

Van Ulden, A. P., and A .A. M. Holtslag (1985), Estimation of atmospheric boundary layer parameters for diffusion applications, *J. Clim. Appl. Meteorol.*, *24*, 1196–1207, doi:10.1175/1520-0450(1985)024<1196:EOABLP>2.0.CO;2.

Viterbo, P., A. Beljaars, J. F. Mahfouf, and J. Teixeira (1999), The representation of soil moisture freezing and its impact on the stable boundary layer, *Q. J. R. Meteorol. Soc.*, *125*, 2401-2426, doi:10.1002/qj.49712555904.

Vogelezang, D. H. P., and A. A. M. Holtslag (1996), Evaluation and model impacts of alternative boundary-layer height formulations, *Boundary Layer Meteorol.*, *81*, 245–269, doi:10.1007/BF02430331.

Walsh, J. E., W. L. Chapman, V. Romanovsky, J. H. Christensen, and M. Stendel (2008), Global Climate Model Performance over Alaska and Greenland, *J. Clim.*, *21*, 6156–6174, doi:10.1175/2008JCLI2163.1.

van de Wiel, B. J. H., R. J. Ronda, A. F. Moene, H. A. R. de Bruin, and A. A. M. Holtslag (2002), Intermittent turbulence and oscillations in the stable boundary layer over land. Part I: A bulk model, *J. Atmos. Sci.*, *59*, 942–958, doi:10.1175/1520-0469(2002)059 < 0942:ITAOIT 2.0.CO2.

Zhang, T., K. Stamnes, and S. A. Bowling (2001), Impact of the atmospheric thickness on the atmospheric downwelling longwave radiation and snow-melt under clear-sky conditions in the Arctic and Subarctic, *J. Clim.*, *14*, 920–939, doi:10.1175/1520-0442(2001)014<0920:IOTATO>2.0.CO;2.